Mapping mineralogical heterogeneities at the nm-scale by scanning electron microscopy in modern Sardinian stromatolites: Deciphering the origin of their laminations

Juliette Debrie, Dimitri Prêt, Nicolas Menguy, Imène Estève, Pierre Sans-Jofre, Jean-Paul Saint Martin, Karim Benzerara

To cite this version:

Juliette Debrie, Dimitri Prêt, Nicolas Menguy, Imène Estève, Pierre Sans-Jofre, et al.. Mapping mineralogical heterogeneities at the nm-scale by scanning electron microscopy in modern Sardinian stromatolites: Deciphering the origin of their laminations. Chemical Geology, 2022, 609, pp.121059. 10.1016/j.chemgeo.2022.121059 . hal-03779040

HAL Id: hal-03779040
https://hal.sorbonne-universite.fr/hal-03779040v1

Submitted on 16 Sep 2022

Mapping mineralogical heterogeneities at the nm-scale by scanning electron microscopy in modern Sardinian stromatolites: deciphering the origin of their laminations

Juliette Debrie[1], Dimitri Prêt[2], Nicolas Menguy[1], Imène Estève[1], Pierre Sans-Jofre[1], Jean Paul Saint Martin[3], Karim Benzerara[1]*

[1]Institut de Minéralogie, de Physique des Matériaux et de Cosmochimie (IMPMC) UMR CNRS 7590, Sorbonne Université, Muséum National d'Histoire Naturelle, 4 Place Jussieu75005 Paris, France.

[2]Institut de Chimie des Milieux et Matériaux de Poitiers (IC2MP), Université de Poitiers, UMR CNRS 7285, rue Albert Turpain, Poitiers, France

[3]Centre de recherche en paléontologie de Paris (CR2P) UMR CNRS 7207, Muséum National d'Histoire Naturelle, Sorbonne Université, 8 rue Buffon, 75005 Paris, France

*Corresponding author: Karim Benzerara, IMPMC, Case 115, 4 Place Jussieu 75005 Paris, France. Phone: 33144277542; Fax: 33144273785; karim.benzerara@sorbonne-universite.fr

Highlights

Mineralogical heterogeneities in Sardinian stromatolites were investigated down to the nano-scale

EDXS analyses combined with an innovative data treatment allowed to retrieve ≥ 15 mineral phases

Mg variations in carbonates were observed between successive laminations but also within a single lamination

Mg-enrichment was observed around microfossils and supports the involvement of microbes in the formation of high-Mg calcite

Allochthonous and authigenic clays and sulfate phases were detected. They may be used as paleoenvironmental proxies

Abstract

Stromatolites are found throughout the geological record and have received strong attention because they provide precious information about paleoenvironments and microbial paleobiodiversity. However, while this information is interpreted based on our knowledge about modern analogs, the latter remains incomplete. Here, we investigated the environmental and biological information recorded by modern stromatolites in Mari Ermi, a coastal pond in Western Sardinia that experiences severe seasonal evaporation and large salinity variations. For this purpose, we combined a variety of analytical tools, allowing to characterize the mineralogical composition of these stromatolites from the bulk, centimeter-scale to the nanometer-scale and assess the spatial distribution of the mineral phases. In particular, we used quantified x-ray elemental maps provided by energy dispersive x-ray spectrometry analyses coupled with scanning electron microscopy (SEM-EDXS). These maps were processed using an innovative data treatment allowing (i) mineral phase recognition, (ii) assessment of the mineral formula of each phase and (iii) mapping of their spatial distribution with a spatial resolution down to a hundred nanometers. Overall, this proved as an efficient approach to unravel mineralogical heterogeneities and detect informative mineral phases overlooked by bulk analyses. Mari Ermi stromatolites were mostly composed of magnesian calcite with an average Mg/Ca of ~ 0.1-0.2 as indicated by bulk analyses. However, microscopy observations revealed variable Mg-contents of calcite with a specific distribution, the most Mg-enriched calcites (Mg/Ca up to ~ 0.5) being systematically distributed around microbial remnants. Moreover, Mari Ermi stromatolites comprised an alternation of Mg-richer and Mg-poorer laminae, which paralleled the varying enrichment in microbial remnants of alternating laminae. The combination of SEM-EDXS, focused ion beam milling and transmission electron microscopy allowed to detect several minor phases, hardly or not detected at all by bulk analyses, such as aragonite, a variety of clay minerals as well as a gypsum-like phase. An additional calcium sulfate phase, best interpreted as S-apatite (cesanite), was detected by SEM-EDXS. Overall, this mineral assemblage and its definite spatial distribution record only discrete stages of the evaporation of Mari Ermi lagoon. Moreover, microorganisms seem to have a major control on Mg substitution in calcite. As a result, the dynamics of microbial populations, influenced by the salinity variations induced by evaporation in the lagoons, generates the formation of laminae in Mari Ermi stromatolites.

Keywords: stromatolites; evaporites; mineral mapping; high magnesian calcite; laminations; X-ray fluorescence

1. Introduction

Stromatolites are macroscopically laminated benthic microbial deposits formed by diverse microbial communities (Riding et al., 1991). They are particularly emblematic geobiological materials since they are considered as the oldest evidence of life-mineral interactions, dating up to 3.5 Gyrs ago (Allwood et al., 2006; Dunlop et al., 1978; Walter, 1970). They are found throughout the geological record and have received substantial attention because they potentially provide precious information about microbial paleobiodiversity (Forel, 2013; Forel et al., 2021; Hohl and Viehmann, 2021; Ribbert and Piecha, 2014) and paleoenvironments (Aubineau et al., 2019; Bourillot et al., 2020; Mary and Woods, 2008; Petrash et al., 2016). Yet, assessing how this information is recorded in the chemical, mineralogical, and textural composition of these rocks as well as their microfossil content is not straightforward (Benzerara et al., 2014). First, there is a need to assess the taphonomic processes that affected these more or less ancient materials (De Boever et al., 2017). Additionally, the study of present-day analogs appears crucial to understand the relationships between the mineralogical and chemical composition of stromatolites, their micro- and macro-textures and the biological and environmental conditions prevailing where these microbialites form (Zeyen et al., 2021, 2017) For example, several authors (Al Disi et al., 2021; Ries, 2010; Ries et al., 2008) proposed that the nature of the carbonate mineral phases composing modern stromatolites (e.g., Mg-calcite, aragonite and/or hydromagnesite) is primarily determined by the aqueous dissolved (Mg/Ca) ratio in the solution where they form. Lately, Zeyen et al. (Zeyen et al., 2021) further suggested that water in which stromatolites form, may need to be saturated with an amorphous calcium carbonate (ACC) phase that would precipitate as a precursor phase before transforming to monohydrocalcite, Mg-calcite or aragonite depending on the (Mg/Ca)aq. However, the diversity of these mineral phases, and how they may record environmental variations within one single microbialite remains to be further documented.

Modern microbialites show a great variety of mineralogical and chemical compositions and diverse degrees of preservation of microorganism-mineral assemblages (Couradeau et al., 2013; Eymard et al., 2020; Wacey et al., 2018; Zeyen et al., 2015). Mineralogical assemblages are most often fine-grained and chemical variations can therefore occur at a fine spatial scale.

Diverse analytical techniques such as x-ray diffraction (XRD) or Fourier transform infrared (FTIR) spectroscopy have been used to identify the different mineral phases composing stromatolites. However, it appears challenging to find microanalytical tools that provide mineralogical information at a high spatial resolution, in a quantitative manner and over large areas, which is essential to assess these microorganism-mineral assemblages with statistical significance. Among the state-of-the-art analytical techniques able to generate accurate and precise mineralogical information, µ-XRD appears interesting (Flemming, 2007). However, despite ongoing developments to achieve nm-scale resolutions (e.g. Elmaleh et al., 2018), the spatial resolution of this technique often remains limited to the micrometer-scale, and there is a need to complement the obtained structural information by additional chemical information. Raman microspectroscopy has been increasingly used to generate maps of mineral phases with a spatial resolution better than 1 µm and assess potential correlations between some phases and specific microorganisms in natural communities (Gérard et al., 2013). However, the occurrence of high-intensity fluorescence caused by laser excitation in biogenic carbonates sometimes overwhelms the Raman signal, hindering the identification of individual Raman-active vibrational modes (Guido et al., 2019; Sánchez-Beristain et al., 2010). Micro–X-ray fluorescence (hereafter µ-XRF) is another powerful tool that can rapidly produce bulk elemental maps with a spatial resolution better than 1 µm, allowing to visualize and quantify chemical heterogeneities within a sample (Flude et al., 2017; Winter and Claeys, 2017). Commonly, µ-XRF facilities are available on synchrotron light sources (Aubineau et al., 2019; Sancho-Tomás et al., 2020, 2018), but with limited access. However, the recent developments by Kaskes et al. (2021) demonstrate the potential of high-resolution, qualitative to semi-quantitative element mapping based on XRF maps with lab-based equipment, opening promising perspectives for more routine analyses.

By contrast, scanning electron microscopy combined with energy dispersive X-ray spectrometry (SEM-EDXS) appears as a widespread laboratory-based technique, which allows assessing chemical heterogeneities down to the scale of a few tens of nanometers. It is relatively simple to use and the sample preparation is limited compared with some other techniques, mostly involving polishing and sputtering or evaporation coating. While SEM is very often used for the study of stromatolites, the information provided by EDXS analyses usually remains incompletely exploited, mostly as qualitative data. Yet, several analytical tools have been developed to retrieve quantitative mineralogical maps from SEM-EDXS maps (Graham and

Keulen, 2019; Haberlah et al., 2015; Prêt et al., 2010a). These tools have been applied in the context of material science and geoscience studies (Cosenza et al., 2019; Gaboreau et al., 2017), but not on objects such as stromatolites, to our knowledge. The application of these tools to stromatolites might be challenging. Indeed, when the primary electron beam hits a sample, X-rays are generated from an interaction volume. The size of this interaction volume is a function of the primary energy of the beam, the mean atomic number of the sample and its density. For instance, for a geological sample containing silicates, interaction volumes could reach 2–5 μm^3, with a 20 keV primary electron beam (Graham and Keulen, 2019). Therefore, at such an energy, it may be impossible to accurately identify and map mixtures of very fine-grained phases, which are common in stromatolites. Thus, decreasing the energy of the beam becomes crucial to resolve and visualize submicrometer-sized phase assemblages with an unprecedented accuracy.

Here, we used a combination of analytical tools, including SEM-EDXS, to map from the cm-scale down to the submicrometer scale the mineralogical composition of modern stromatolites collected in the coastal ponds of Mari Ermi, Western Sardinia. This provides a deep insight into the chemical and mineral heterogeneities occurring in stromatolite laminations, the origin of which remains a matter of intense discussion. The morphological and textural description of these stromatolites at a macroscopic and mesoscopic scale has been provided by Saint Martin and Saint Martin 2015. They form in a saline to hypersaline environment where conditions are extremely fluctuating seasonally with almost complete drying of the pond in the summer and flooding during the fall and winter. One primary question was whether these environmental variations could impact the nature of the mineral phases forming over time in the stromatolites. For that purpose, we conducted a multi-scale mineralogical characterization of these stromatolites and discussed the complex processes that affected their formation, in particular inferring how they may be related to biological and environmental drivers.

2. Materials and methods

2.1. Geological setting and samples

Mari Ermi is located on the west coast of Sardinia in the Sinis peninsula (Fig. 1a). Mari Ermi ponds (Mari Ermi North (MEN) and Mari Ermi South (MES)) are two water bodies measuring few hundreds of meters in length, stretching parallel to the shore and separated from each other by a transversal land strip (Fig. 1b). Saint Martin and Saint Martin (2015 provided an extensive description of the regional setting. The microbialites have a cerebroid pustular aspect (Fig. 1c). They are abundant on and close to the shores of the ponds and become scarce in their center. During the dry season, they become subaerial, whereas they are immersed and covered by green microbial biofilms during the wet season. These microbialites are macroscopically laminated and are therefore defined as stromatolites. The laminated, microbialitic part grows on hard substrates, such as limestone pebbles. In cross-sectioned samples, one can clearly distinguish a non-stromatolitic part (the substrate) from the stromatolitic part accreting on top of it (Fig. 1d). Samples were observed *in situ* and collected in September 2016, when ponds were completely dried as well as in June 2018, when ponds were filled with water.

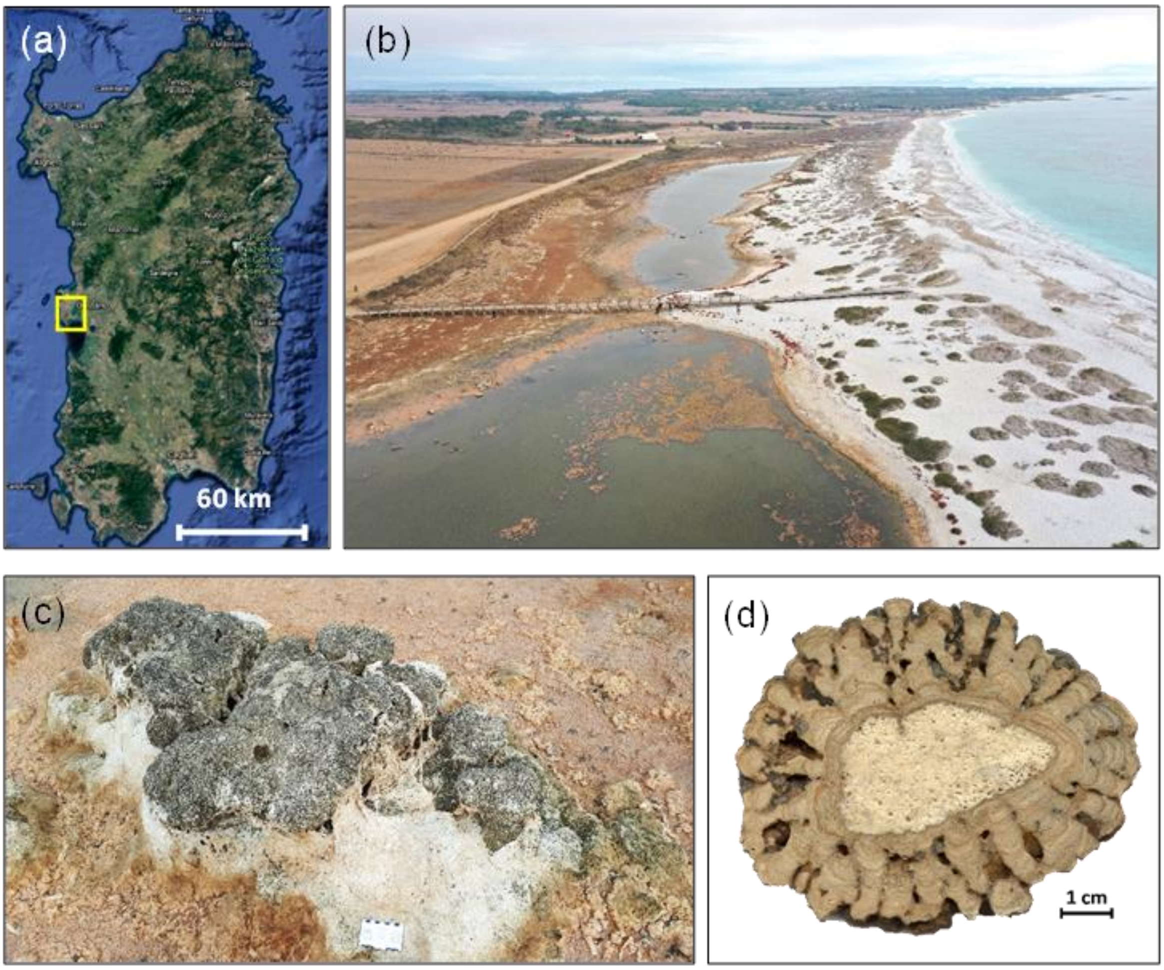

Fig. 1 Mari Ermi geographical location and microbialite features. (a) Satellite image of Sardinia. The yellow square indicates Mari Ermi coastal ponds. (b) Drone picture of Mari Ermi North. Note that the coastal ponds (to the left) are separated by a land strip from the Mediterranean Sea. (c) Macrofacies Mari Ermi stromatolites. (d) Polished slab section of Mari Ermi stromatolite.

2.2. Bulk chemical & mineralogical characterization

The stromatolitic part was hand-separated from the substrate beforehand. About 10 g of the stromatolitic part was finely ground in ethanol and homogenized in an agate mortar. Aliquots of the same powdered sample were used for the different bulk chemical analyses, i.e., X-ray diffraction (XRD) Fourier transform infrared (FT-IR) spectroscopy and Inductively coupled plasma atomic emission spectroscopy (ICP-AES).

2.2.1. Bulk chemical analyses

Chemical compositions (in oxide wt%) of major and minor elements were measured by the *Service d'Analyses des Roches et Minéraux* (SARM, Centre de Recherches Pétrographiques et Géochimiques, Nancy, France). Major element analyses were performed using an ICP-AES ICap 6500 (Thermo Fischer) after alkali fusion of rock samples with $LiBO_2$ followed by dissolution in HNO_3. The precision of the measurements was between 1% and 25%, depending on their concentrations (Table S1).

2.2.2. X-ray diffraction

The bulk mineralogical composition of stromatolites was determined by XRD. About 1 g of each stromatolite sample was deposited on an aluminum sample holder. XRD measurements were performed using a Panalytical X'Pert diffractometer equipped with a cobalt anode (Co-Kα). Data were recorded at 40 kV and 40 mA in the continuous-scan mode between 5 and 80° (2θ) with a step of 0.016° and a total counting time around 4 h. Diffractograms were analyzed using the PANalytical X'Pert Highscore software for background subtraction, peak finding, and matching with XRD patterns of reference compounds. Reference patterns were obtained from the international crystal structure database (ICSD, Fachinformationszentrum Karlsruhe, Germany; US Institute of Standards and Technology, USA). Lebail refinement was computed using the FullProf software and the following calcite cell parameters a = b = 4.9896 Å and c = 17.061 Å were implemented as initial parameters.

Mg substitution was assessed based on the calcite *c* parameter and the relationship derived by Dos Santos et al. (2017): $c = - 1.8603*x(Mg) + 17.061$, where x(Mg) is the molar fraction of Mg replacing Ca.

2.2.3. Fourier transform infrared spectroscopy analyses

For FTIR spectroscopy analyses, 2.5 mg of stromatolite powder were mixed with 300 mg of potassium bromide (KBr) and ground together in an agate mortar. A KBr pellet was prepared for each sample using a vacuum press under 8 tons of pressure for 1 minute. Pellets were placed overnight in a drying oven (95 °C) to remove the adsorbed water vapor and were pressed a second time. Transmission spectra were recorded between 400 and 4000 cm^{-1}, using a Nicolet 6700 FTIR spectrometer.

2.3. Petrographic thin section preparation

Petrographic thin sections were prepared for light and electron microscopies. First, the stromatolite samples were cut in half using a circular saw. One half was embedded in a polyester resin (GBS1, Aeri SAS) under vacuum, then sawn, polished with alumina suspension (0.1 µm grain size) and glued on a glass slide with Araldite (HUNTSMAN). Finally, it was thinned by polishing down to 30 µm in thickness. The resin mainly contains C and O elements and possible N as amine groups in the resin hardener.

2.4. Light microscopy

Petrographic thin sections measuring 30 µm in thickness were observed using a Leica DM 2500P light microscope (IMPMC, Paris). One section was fully imaged in transmitted light using a macro-apotome Zeiss Axio Zoom.V16 motorized stereo microscope (Institut de Biologie Paris-Seine, Paris). This provided images at a 1000 × magnification (corresponding to ~1 µm/pixel) over a large area.

2.5. X-ray fluorescence microscopy

The spatial distribution of chemical elements was determined at the near-surface of a non-embedded polished rock slab measuring 5 cm in thickness by micro X-ray fluorescence (µXRF) using a Bruker M4 Tornado µXRF scanner (Bruker nano GmbH, Germany) at the Laboratoire Géoscience Océan (Laboratoire Bretagne Occitanie, Ifremer, Brest). The X-ray tube was a Rh anode operating at 599 µA with an accelerating voltage of 50 kV. Chemical maps measured 1440 x 1820 pixels, with a pixel size of 40 µm, and a dwell time of 6 ms. The individual µ-XRF pixel spectra were quantified by removing the background and applying a fundamental parameter algorithm based on the Sherman equation (Sherman, 1955; Rousseau, 2013). As a standardless approach was used, the chemical maps were semi-quantitative with measured concentrations being proportional to the actual ones but with some potential absolute errors on some elements. A binning of 2 x 2 pixels (resulting in a pixel size of 80 µm) was used allowing to reach a signal-to-noise statistics satisfying for quantification, except for Mg for which a binning of 8 x 8 pixels was chosen, resulting in a pixel size of 320 µm. Finally, all the semi-quantitative chemical maps were denoised to improve the signal-to-noise ratio, color encoded and sometimes histogram equalized to enhance the contrast (Russ, 1999) using an in-house *ImageJ* plugin.

2.6. Scanning electron microscopy

Petrographic thin sections were carbon-coated to make their surface conductive for electrons. They were fixed to an aluminum holder using copper tape Petrographic thin sections were observed by scanning electron microscopy (SEM). Since they measure 30 µm in thickness, only part of the thinned rock sample and not the underlying glass slide was probed by SEM-EDXS.

2.6.1. Back-scattered electron scanning electron microscopy (BSE -SEM) mosaics

A high resolution centimetric mosaic (3.46 × 4.14 cm^2, 231 000 × 276 000 pixels, pixel size of 150 nm), covering most of one stromatolite sample was built from 77 x 92 tiles. The total acquisition time was about 78 hours. Tiles were acquired using a SEM-FEG Zeiss Crossbeam Neon40 EsB) equipped with the Atlas5 module at IMPMC, with an acceleration voltage of 15 kV, a working distance of 12 mm and a dwell time of 3.0 µs per pixel. The Atlas5 module allows the automatic acquisition of multi-detectors large mosaics within a correlative space, with an auto-focus and auto-stigmatism correction for each tile. The acquired mosaic is then stitched by an Atlas5 tool to reach perfect tiling.

2.6.2. SEM-EDXS quantitative chemical maps

The elemental composition and texture of the samples were studied using a JEOL JSM-7900F SEM-FEG equipped with a BRUKER Quantax FlatQuad annular EDXS detector at IC2MP. Acquisition parameters were selected to achieve (1) the best energy resolution (124 eV) of the EDXS detector, needed for an accurate deconvolution of interfering emission lines, (2) a high

X-ray counting statistics to allow a precise quantification of the maps and (3) optimize the spatial resolution. The hypermaps were performed with the following analytical conditions: an accelerating voltage of 5 kV, a probe current of 2.15 nA, a working distance of 10.9 mm, a dwell time per pixel of 35 ms and pixel sizes of 230/61 nm for large/small hypermaps with a live beam drift correction. The FlatQuad detector allows fast acquisition of large hyperspectral maps (e.g., 1400 x 1050 pixels in 14 hrs) with a convenient counting statistics of 15 kcps per EDXS spectrum on a single pixel. This is achieved based on a large solid angle of detection (~1 str) and a thin Mylar window allowing low energy X-ray detection. Moreover, the use of such an annular detector over the sample cancelled the effects of potential local relief at the surface of the sample which would otherwise induce well-known quantification errors (tilt effect, shadowing) if only one directional EDXS/WDS detector was used instead. The accelerating voltage was the most important parameter to tune because it controls the spatial resolution of the acquired image (Hombourger and Outrequin, 2013; Fournelle et al., 2016). Here, the diameter of the BSE and X-ray emission volumes is estimated to be smaller than 380 nm for calcite and 700 nm for resin at 5 kV on the basis of the Kanaya-Okayama equation (Kanaya and Okayama, 1972). By contrast, the probe diameter has a minor effect since it is smaller than the probed volume by several orders of magnitude. The probe diameter controls the spatial resolution of in-lens secondary electron images and has been estimated down to 5.8 nm for the acquisition parameters used. A specific library of standards with synthetic and natural oxides and silicates (calcite, apatite, albite, augite, celestine, diopside, forsterite, garnet, orthose, TiO_5, almandine, and anhydrite) were acquired using the same parameters. Then, each EDXS spectrum for each pixel was quantified using the ESPRIT, Bruker software based on the following procedure: 1) X-ray background generated by Bremsstrahlung was modeled accounting for X-ray absorption by the sample/carbon coating layer / detector window (Zanetta et al., 2019) and removed to obtain unbiased elemental maps in comparison with raw count maps (Donovan et al., 2021) 2) Quantification by a standard-based extended Pouchou-Pichoir (XPP) matrix correction was applied to provide a weight percentage for each element per pixel. The very small X-ray emission volumes achieved at this low voltage decreased the heterogeneity of the probed volume, allowing more robust element quantification. Most of the light element, at least the most abundant ones (e.g., C, O, F, N) were quantified. To back-control the list of detected elements and the robustness of spectrum quantification, we extracted manually the EDXS spectrum of few different phases from one pixel as well as from an area with clear porosity (Fig. S1). Some quantifications issues were encountered: 1) the overlap of the Si with the Sr peaks induced inaccurate quantification of Sr for Si-bearing minerals. However, we were able to discriminate true Sr hotspots from false Sr-/ true Si-hotspots by comparing Si and Sr maps. 2) The background removal procedure implemented in the Bruker software did not account for the large range of X-ray take-off angles associated with the FlatQuad annular detector but instead considered a usual mean take-off angle. This hinders a perfect removal of the background at low energy when interferences of emission lines occur within the low energy range. As a result, only semi-quantitative concentrations maps are generated for the low energy emission lines of N, F (based on K emission lines), Co, Mn and Fe (based on the L emission lines) and Ba (based on M emission line). 3) The C and O contents are measured on the basis of a calcite standard that induces slight errors on oxygen contents measured for silicates. Before further numerical treatment, all the quantitative maps were denoised, color encoded and sometimes contrast-enhanced by equalization using the in-house *ImageJ* plugin detailed above.

2.6.3. SEM-EDXS hypermaps mosaic

A mosaic (14 × 0.91 mm^2; 20,500 × 15,375 pixels) was built from 41 hypermaps (pixel size of ~ 680 nm) acquired by a JEOL® JSM-7900 SEM, with an acceleration voltage of 8 kV (X-ray emission volume radius around 520 nm in calcite), a probe current of 2.18 nA, at a working distance of 10.9 mm, and a dwell time of 64 µs per pixel. This hypermap mosaic provides a qualitative chemical map (i.e., raw count maps), extending across the full stromatolite thickness, with a spatial resolution drastically improved in comparison with µXRF.

2.6.4 Translating elemental maps into quantitative mineralogical maps

Mineralogical maps, i.e. the spatial distribution of the diverse mineral phases, were created for two surface areas of 18 x 14 µm^2 and 330 × 230 µm^2 with a pixel size of 61 or 230 nm, respectively. The processing of these maps was based on mineral identification methods that accommodate phase mixtures and solid solutions and are implemented in the *in-house* µPhaseMap software (Prêt, 2003). This methodology consists in identifying the mineral phases composing the analyzed area based on step by step projections of the scanned elemental composition points into ternary scatterplots. This allows to visualize contrasting elemental compositions for all the mineral phases. Each axesof the ternary diagram represents a 100% content of an element or a combination of elements. Since, three chemical elements are not enough to discriminate most rock-forming minerals, more complex ternary plots are used, where different element concentrations can be added, subtracted, divided, or multiplied to calculate the coordinate along one axis of the plot. A sequence of successive ternary projections is needed to discriminate all the rock-bearing minerals, especially when they show close stoichiometries. Then, we identify several clusters of pixels with similar compositions within each ternary plot. Here, the amount of pixels located at the same position within the scatterplot is encoded by a Log-3-band color scale that facilitates the recognition of few-pixels clusters (*i.e.*, mineral corresponding to trace phases) as well as hundreds-of-thousands-pixel clusters (major phases) (Prêt et al., 2010c). Each cluster represents the chemical compositional field of one mineral phase endmember. For mineral recognition, the calculated stoichiometry of the phase represented by a cluster is compared with a database of different theoretical endmembers, the composition of which is displayed as a red dot in the ternary plots (Table S2). Mixtures of different phases and solid solutions (highlighted by dashed arrows and dashed lines, respectively) appear as pixels along lines in between the endmembers within the ternary projections. Then, outlining the clusters of interest by hand-drawn polygons (a procedure called segmentation) allows to either back-project the selected pixels on a phase map or re-plot them into another scatterplot. The calculation of the mean mineral unit formula of a phase is achieved by segmenting pixels using restricted polygons (indicated as black squares) that represent the purest chemical analyses of the detected phase. More details are provided by (Prêt, 2003; Prêt et al., 2010d, 2010a; Gaboreau et al., 2017) who successfully demonstrated the capability of this approach to properly identify all the minerals (and detect some unknown ones) in well-known porous materials such as the worldwide reference of compacted clay targeted for nuclear waste storage or cementeous materials for which an extended literature combining all the known bulk methods is available. This proved that it is possible to reach a robust mineral identification by careful analysis of local chemical compositions in a first step. Additional techniques may be needed for refining the identification of e.g., various polymorphs that cannot be distinguished based on their stoichiometry alone.

2.7. Focused ion beam (FIB) milling

The mineral maps generated by SEM-EDXS allowed localizing some minor nanophases identified as areas of interest that were subsequently cut by FIB and further studied by TEM. Four ultrathin electron-transparent foils were cut from a stromatolite section. This was achieved by focused ion beam milling using a FEI Strata Dual-beam 235 instrument operating at 30 kV and 5 nA following the FIB lift-out method as described by Benzerara et al.,(2005. Before milling, a platinum strap was deposited onto the region of interest of the sample. After *in situ* transfer to a copper grid, the foil was thinned down to around 100 nm with a Ga$^+$ beam current of about 100 pA and at glancing angle.

2.8. Transmission electron microscopy (TEM)

FIB foils were analyzed using a JEOL 2100F transmission electron microscope (TEM) operating at 200 kV. This microscope is equipped with a FEG, an ultra-high resolution pole piece, a JEOL EDXS detector with an ultrathin window allowing the detection of light elements, and a scanning TEM (STEM) device, which allows Z-contrast imaging in high angle annular dark field (HAADF) mode. Elemental mapping was acquired by EDXS in the STEM mode, using the JEOL Analysis Station software. Selected area electron diffraction (SAED) patterns were recorded to refine the identification of mineral phases, discriminate the different polymorphs and assess their crystallinity. SAED patterns were processed using the *Image J* software in order to measure d-spacings. SingleCrystal software 3.1 was used to index diffraction patterns.

3. Results

3.1. Bulk mineralogical characterization

Bulk XRD analyses showed that Mari Ermi stromatolites are mostly composed of magnesian calcite (Fig. 2a). LeBail refinement of the Mg-calcite cell lattice parameters assessed that a = b = 4.939113 Å and c = 16.859440 Å. Mg substitution (expressed as Mg/[Mg+Ca]) was estimated from the *c* parameter at 10.8% (Dos Santos et al., 2017). It is equivalent to a molar Mg/Ca ratio of 0.12. Additional minor peaks were detected at (2θ)37 °, (2θ)53 ° and (2θ)78 ° for halite and (2θ)24 °, (2θ)31 ° and (2θ)76 ° for quartz. FTIR analyses were consistent with XRD analyses (Fig. 2b). Indeed, the main vibrational bands at 715 , 877 , 1428 , 1803 and2519 cm^{-1} were respectively attributed to the ν_4, ν_2, ν_3 (ν_1 + ν_4) and (ν_1 + ν_3) bands of calcite (, 1974). By comparison with reference spectrum, weak bands at 1023 and 1153 cm^{-1} reveals some Mg substitution in calcite. In addition, we noticed the presence of small bands at 1082 and 1457 cm^{-1}, suggesting the presence of aragonite based on a comparison with reference spectra from the RRUFF database.

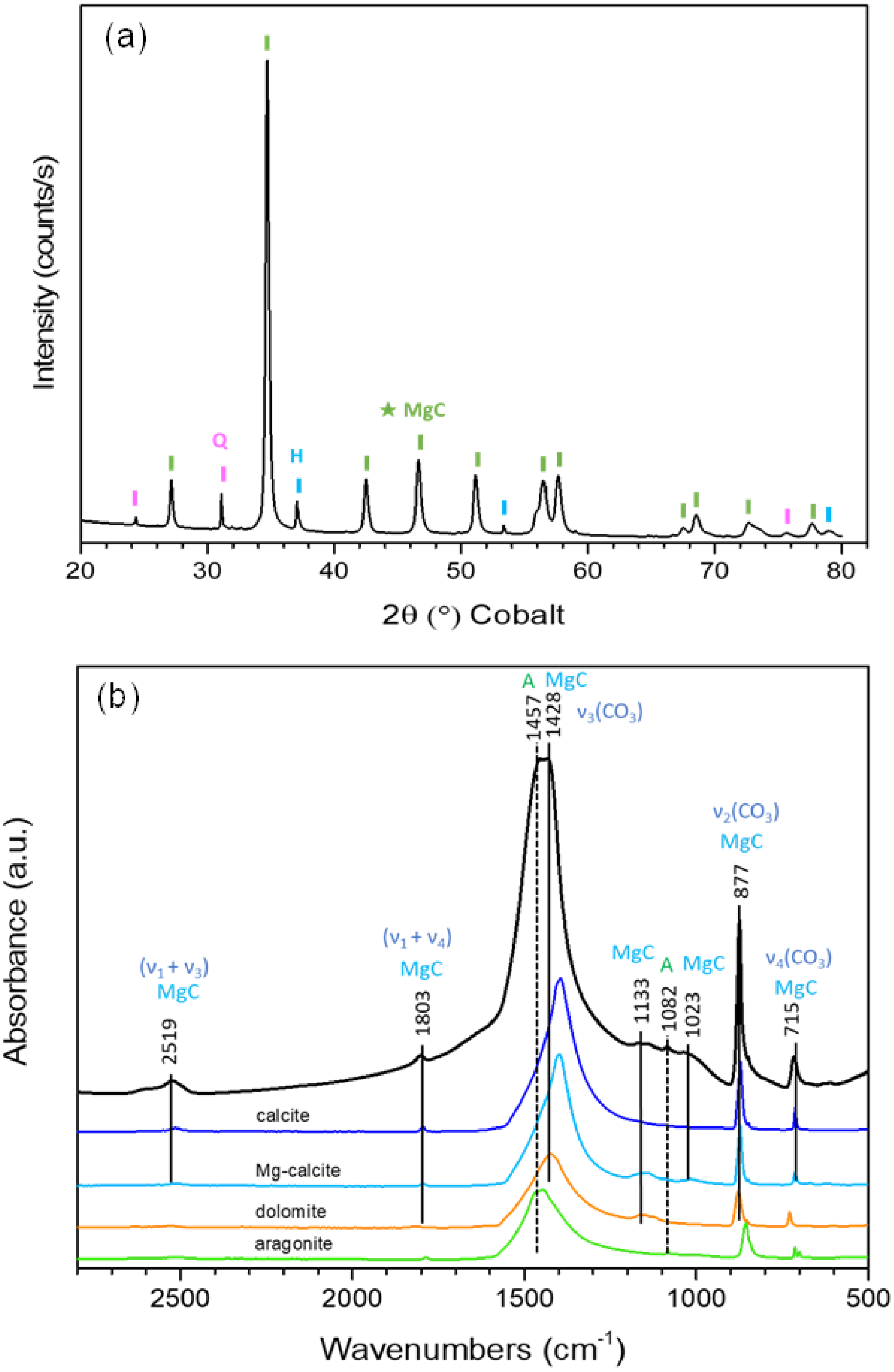

Fig. 2 Bulk analyses of Mari Ermi stromatolites. (a) Bulk X-ray diffraction pattern. Magnesian calcite (MgC) in green, Halite (H) and Quartz (Q) in pink are identified. The green star indicates that MgC is the main phase. (b) FTIR spectrum in the 500-2800 cm^{-1} wavenumber range. Reference spectra of aragonite (green), MgC ($Ca_{0.99}Mg_{0.01}CO_3$) in cyan, dolomite (orange), and calcite (blue) from the RRUFF database are shown for comparison. Vertical lines at 2519, 1803, 1428, 1133, 1082, 1023, 877 and 715 cm^{-1} are indexed as bands characteristics of Mg-calcite. The shoulder at 1457 cm^{-1} is indexed as aragonite. Also note the 1082 cm^{-1} band, characteristic of aragonite.

Bulk chemical analyses of major elements are shown in Table 1. The samples from MEN and MES have similar chemical compositions: Ca (CaO mass content of ~ 43%), Mg (MgO mass content of ~5%), and Si (SiO_2 mass content of ~2 -3%) are the most abundant chemical elements in the samples (Table 1) followed by sodium, aluminum, and iron. Moreover, the low Al mass content (Al_2O_3 mass content of ~0.5 %), suggests that samples are dominated by authigenic phases and only little affected by detrital contamination. Assuming that most of the Mg is contained in the magnesian calcite, bulk chemical analyses give a Mg/Ca ratio equal to ~ 0.2, which is close to the Mg/Ca ratio determined independently by XRD.

Table 1. Major element compositions of microbialites from Mari Ermi lagoons obtained by bulk chemical analyses (LOI = loss of ignition)

Sample	**SiO** (wt %)	**Al2O3** (wt %)	**Fe2O3** (wt %)	**MgO** (wt %)	**CaO** (wt %)	**Na2O** (wt %)	**K2O** (wt %)	**MnO** (wt %)	**TiO2** (wt %)	**Mg/Ca** (atom)	**LOI** (wt %)	**Total**
SAR16-MES-1	2.72 ± 0.2	0.46 ± 0.09	0.27 ± 0.05	4.8 ± 0.5	43.4 ± 0.9	0.91 ± 0.09	0.12 ± 0.04	0.04 ± 0.04	0.025 ± 0.006	0.19 ± 0.02	46.18	99.0
SAR16-MEN-1	2.24 ± 0.2	0.5 ± 0.1	0.46 ± 0.09	5.2 ± 0.1	42.6 ± 0.8	0.9 ± 0.1	0.19 ± 0.04	0.0869 ± 0.04	0.024 ± 0.008	0.205 ± 0.05	46.29	98.7

	Si (wt %)	**Al** (wt %)	**Fe** (wt %)	**Mg** (wt %)	**Ca** (wt %)	**Na** (wt %)	**K** (wt %)	**Mn** (wt %)	**Ti** (wt %)	**Mg/Ca** (atom)
SAR16-MES-1	1.2	0.25	0.21	2.9	30.8	0.7	0.12	0.03	0.015	0.16
SAR16-MEN-1	1	0.28	0.36	3.15	30.3	0.7	0.156	0.067	0.0144	0.17

3.2. Microscopy analyses at large scale

Transmitted light microscopy observations (Fig. 3a) and SEM mosaics (Fig. 3b & Fig. S2) were achieved over relatively large (~12 cm^2) areas to obtain an overview of the texture and distribution of mineral phases. The sample is composed of a non-laminated substrate overlain by the stromatolite *sensu stricto,* which shows a laminated mesofabric, with a typical alternation of dark and bright laminae as observed by both light microscopy (Fig. 3a) and BSE-SEM (Fig. 3b). We note that laminae seen as bright by light microscopy (Fig. 3a) appear dark in BSE since they are filled with organic-rich material (resin and/or organic matter) (Fig. 3b) and conversely. Thereafter, bright and dark will refer to the contrast observed in light microscopy unless mentioned otherwise. These laminae are typically seen as a succession of growth stages.

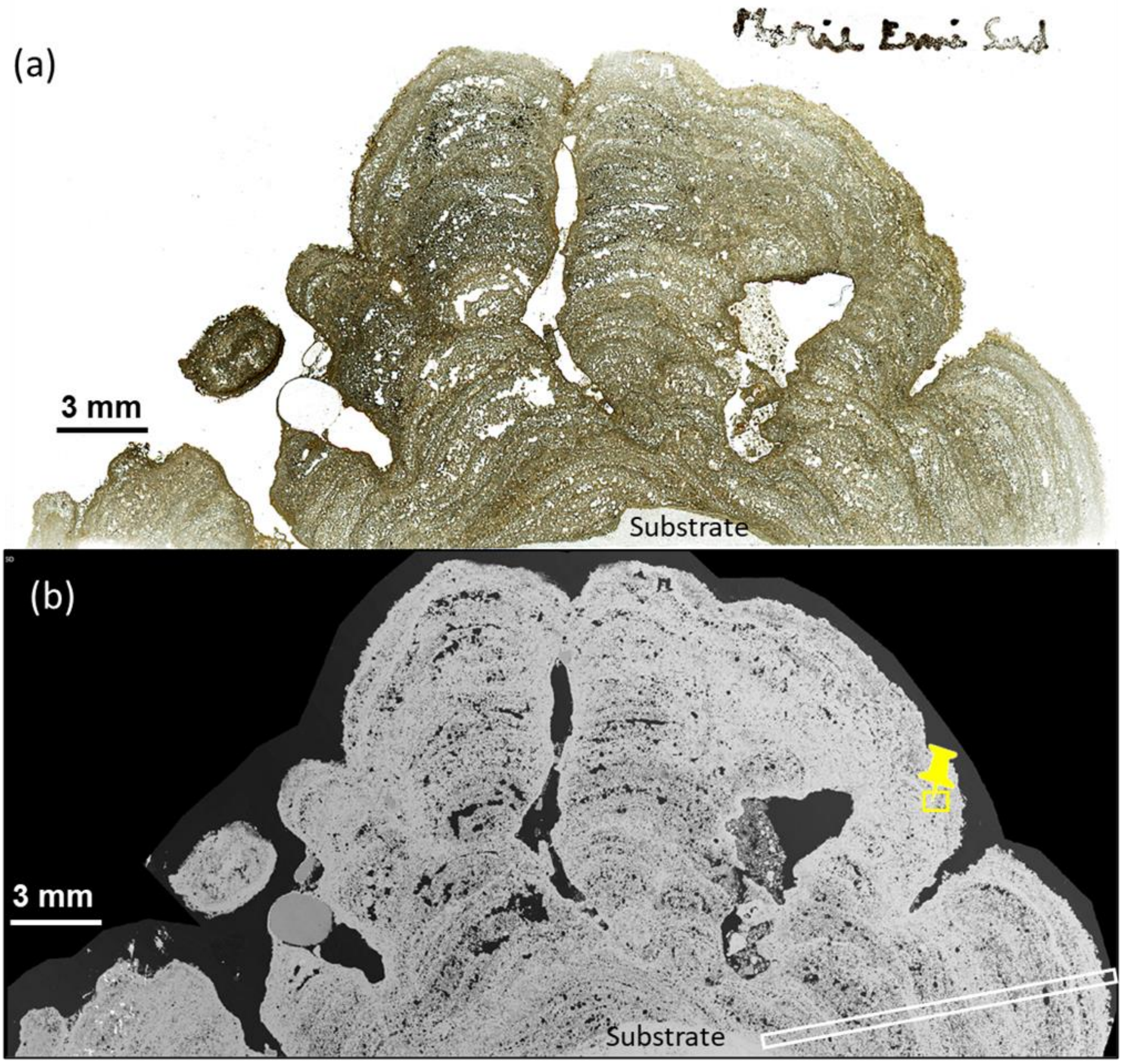

Fig. 3 Correlative light microscopy and scanning electron microscopy mosaics. (a) Light microscopy mosaic acquired on a thin section of a Mari Ermi stromatolite (b) SEM-BSE mosaic acquired on the same sample as in (a). The yellow pin and the white rectangle indicate the areas chosen for the EDX hypermaps-mineral mapping (Figs. 6 & 15) and the EDX mosaic, respectively (Fig. S4). Note that the thick and porous dark laminae in BSE correspond to the light brown ones in optical microscopy, whereas the thin and dense light laminae in BSE correspond to the dark brown ones in optical microscopy.

The lowest basal lamina, directly above the substrate, is very dense (Fig. 4a-b**)**, i.e. almost without any porosity as assessed by SEM, making it different from the overlying laminae. Bright laminae contain numerous upward-oriented filaments (Fig. 4c-d**)**. They are particularly abundant in the upper part of the stromatolite. These filaments, interpreted as microbial remnants, measure ca. 10-15 µm in diameter and 100 to 150 µm in length, and they appear darker in BSE than the carbonate matrix surrounding them. They show variable degrees of lithification, poorly to densely cemented, and often contain elongate voids (Fig. 4e). The voids are sometimes filled by micrite and other recrystallized grains (Fig. 3-4). Circular sections of microfossils with diameters of ca 10-20 µm were also observed (Fig. 4g). While they could be the same filamentous fossils as the ones mentioned above but cut perpendicularly, they seem to exhibit a higher degree of encrustation by carbonates. By contrast to the bright laminae, dark laminae exhibit carbonate phases with only very few filamentous microfossils (Fig. 4d).

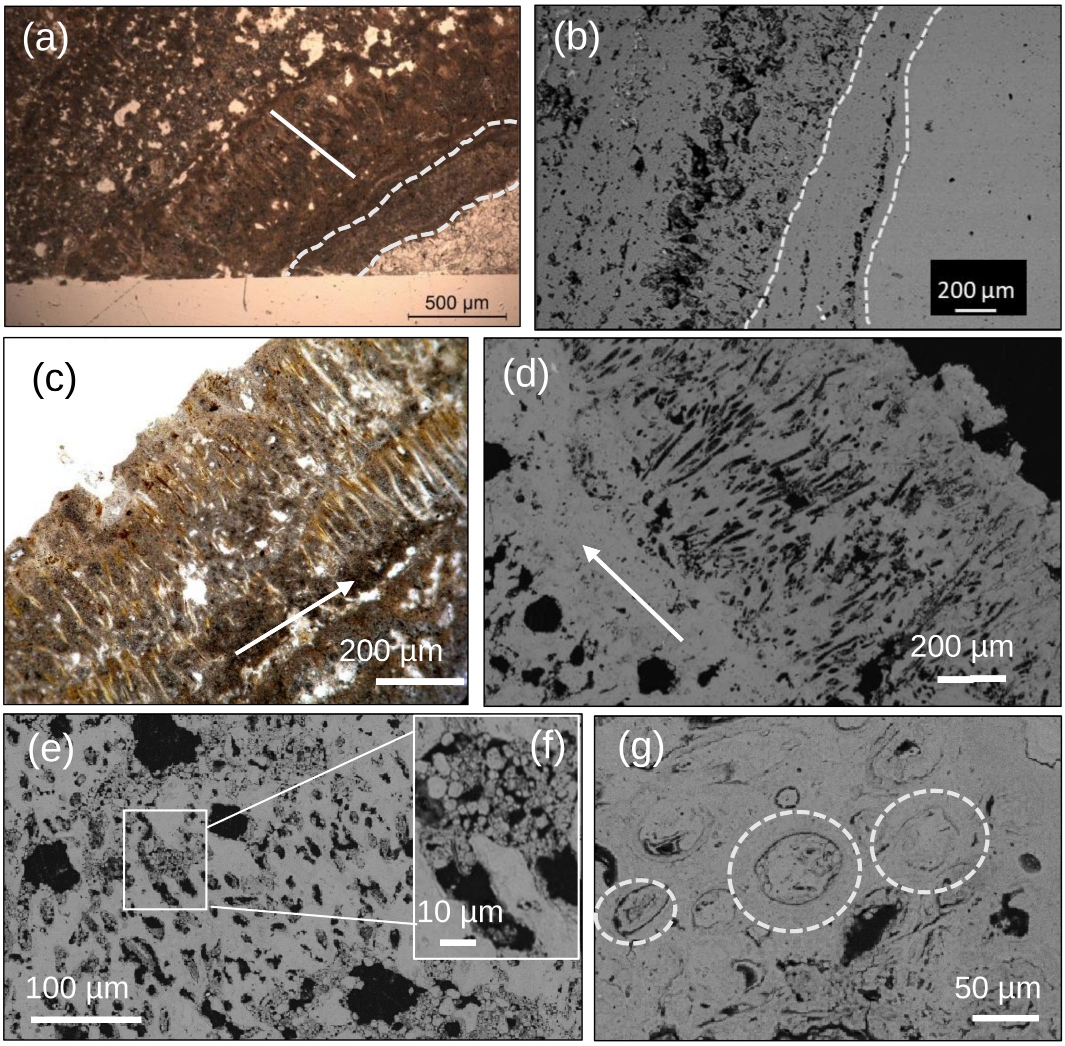

Fig. 4 Light microscopy and scanning electron microscopy observations of Mari Ermi stromatolites. (a) Light microscopy image of the bottom part of the stromatolite. On the bottom right hand, the substrate appears as a bright and almost transparent area. It is overlain by a dense lamina (highlighted by white dotted lines). A succession of filamentous layers overlain this first lamina. (b) SEM-BSE image of the same area as shown in (a), rotated by 90° counterclockwise. The white dotted lines show that the first laminated layer is denser and contain few or no microfossils. (c) Light microscopy image of the top part of the stromatolite. Detail of successive filamentous layers that exhibiting a cyanobacteria sheath-like structure, probably already fossilized. (d) SEM-BSE image of the same area as shown in (c) rotated by 90° clockwise. Filamentous cyanobacteria sheaths filled by resin and/or organic matter appear in dark and are contained within bright laminae, whereas dark laminae (white arrow) appear denser (i.e., with little to no porosity). (e) SEM-BSE image showing filamentous microfossils poorly entombed in the carbonate matrix. The voids are filled with carbonate and non-carbonate particles. (f) Close-up of (e) showing micrite filling up the voids associated with microfossils. (g) SEM-BSE image showing microfossils entombed in the carbonate matrix (circled by white dotted lines).

Additionally, a µXRF map (~42 cm^2) was measured to spatialize the chemical element distribution over a whole section of a Mari Ermi stromatolite with a 80 µm spatial resolution for most elements and 320 µm for Mg (Fig. 5). Semi-quantitative maps of Al, Ca, Cl, Fe, K, Mg, Mn, Na, S, Si, and Sr, obtained by µ-XRF, evidenced chemical variations in the stromatolitic laminae. The stromatolitic part is composed of Mg-calcite and appears chemically distinct from the Mg-poor calcitic substrate. Assuming that all Mg is contained within calcite, the average Mg/Ca ratio estimated in the stromatolitic part is ~ 0.1 (Table 2), consistently with the value assessed by XRD. The high Mg content (mapped with a 320 µm spatial resolution) correlates with the highest grey values of the optical images, meaning that high Mg-carbonate are contained within bright laminae (Fig. S3**)**. The suspected correlation between bright/dark laminae and Mg content was further confirmed at a higher spatial resolution (0.8 µm) based on an EDXS mosaic acquired over an extended area, spanning across laminae, from the substrate to the top of the stromatolite (Fig. S4). It confirms presence of higher Mg concentrations within bright laminae, i.e., laminae containing filamentous microfossils. Si-rich grains are inferred to represent either quartz, feldspar or clays and Si average content over the whole XRF map (~0.7 wt.%) (Table 3) was in the same order of magnitude as the one provided by bulk analyses. Si-rich grains are mostly present in dark laminae as shown by the negative correlation between optical grey values and Si concentration (Fig. S3). The highly correlated distributions of Cl and Na suggest the presence of halite. However, some surficial halite patches detected by XRF might be local artefacts of sample preparation, hiding emission lines of other elements (e.g. Ca, Mg, and S) contained beneath, within the sample. Although Fe, Mn and Sr yielded low count rates, they showed particular distributions: Mn was mainly distributed at low concentration in the upper part of the stromatolites; Fe was abundant in the basal dense laminae, while in the rest of the stromatolite, some Fe-rich grains were associated with Si grains. Sr was significantly enriched in the stromatolite compared to the substrate. Contrary to Mg and Si that show strong correlation with bright and dark laminae respectively, Fe, Mn, S and Sr are not uniquely correlated with bright or dark laminae. This suggests that these elements are contained within both dark and bright laminae and may be carried by different mineral phases. Thus, a more spatially resolved mineral study of the different phases composing Mari Ermi stromatolites was conducted to understand the chemical mineral composition of the stromatolitic laminae.

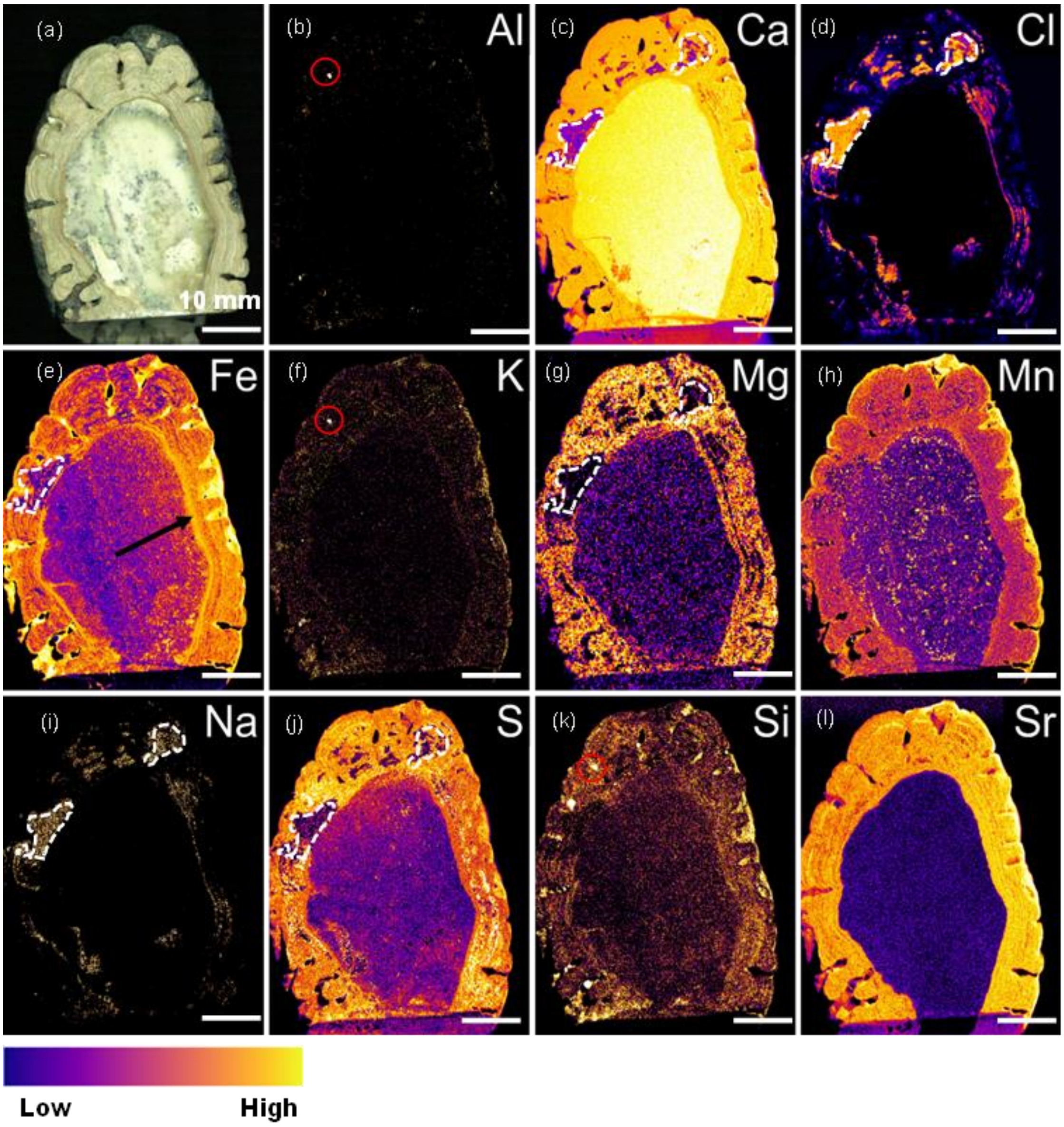

Fig. 5 Micro X-ray fluorescence analysis of a Mari Ermi stromatolite. (a) Photograph of a polished section of a whole stromatolite showing the substrate in the center and the stromatolitic part surrounding it. (b)-(l): µ-XRF quantitative maps of Al, Ca, Cl, Fe, K, Mg, Mn, Na, S, Si and Sr. Some spots are rich in Al and Si, (red dotted circles). The white dotted lines highlight a surficial Na- and Cl-rich deposits, which likely absorbs most x-ray emitted beneath and therefore prevents the detection of other elements such as Ca, Mg and S. Quantification of the elements is encoded in false color following a color scale from dark blue (absence) to bright yellow (maximum concentration).

Table 2. Chemical composition associated with the area outlined by a yellow line in the XRF map.

Element	**Mass [wt%]**	**abs. error [%] (2 sigma)**
Aluminium	0.300	0.001
Calcium	20.559	0.003
Carbon	6.82	/
Chlorine	7.786	0.003
Iron	0.1188	0.0001
Magnesium	1.243	0.005
Manganese	0.0021	0.0001
Oxygen	30.43	/
Potassium	0.1224	0.0003
Silicon	0.613	0.001
Sodium	6.28	0.03
Strontium	0.1135	0.0001
Sulfur	0.4724	0.0006
Mg/Ca	**0.0996**	0.0008
Total	74.86	

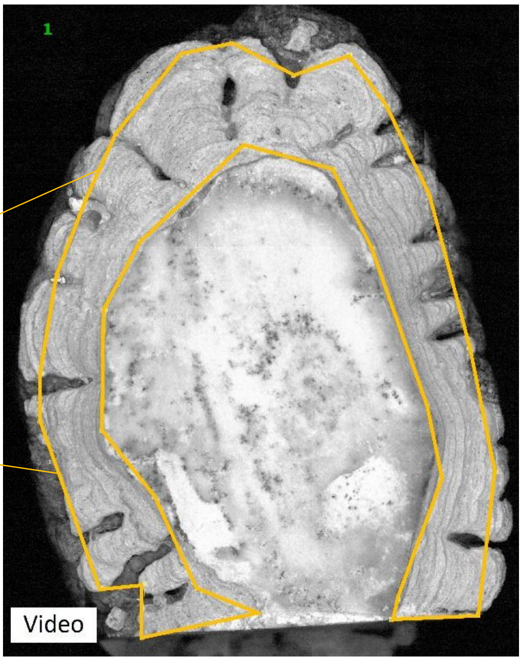

3.3. High resolution quantitative SEM-EDXS chemical and mineral phase mapping

Quantitative SEM-EDXS maps were measured in an area close to the top surface of the stromatolite, to further investigate chemical heterogeneities, including the local enrichments in Mg, Si, Sr and S evidenced by µ-XRF measurements. The BSE image of the chosen area (Fig. 6) shows the presence of two bright laminae alternating with two dark laminae. The bright laminae contain abundant microfossils, completely or partially entombed by carbonates. An intensely bright phase can also be noticed by SEM, distinguishable from the rest of the carbonate matrix in the upper left-hand corner of the image. It consists of a Ca-carbonate phase with ca. 1 wt. % Sr (Table 3). This phase has little to no porosity as suggested by the fact that the sum of the analyzed element concentrations in this phase is about equal to 100%, according to Prêt et al. (2010b).

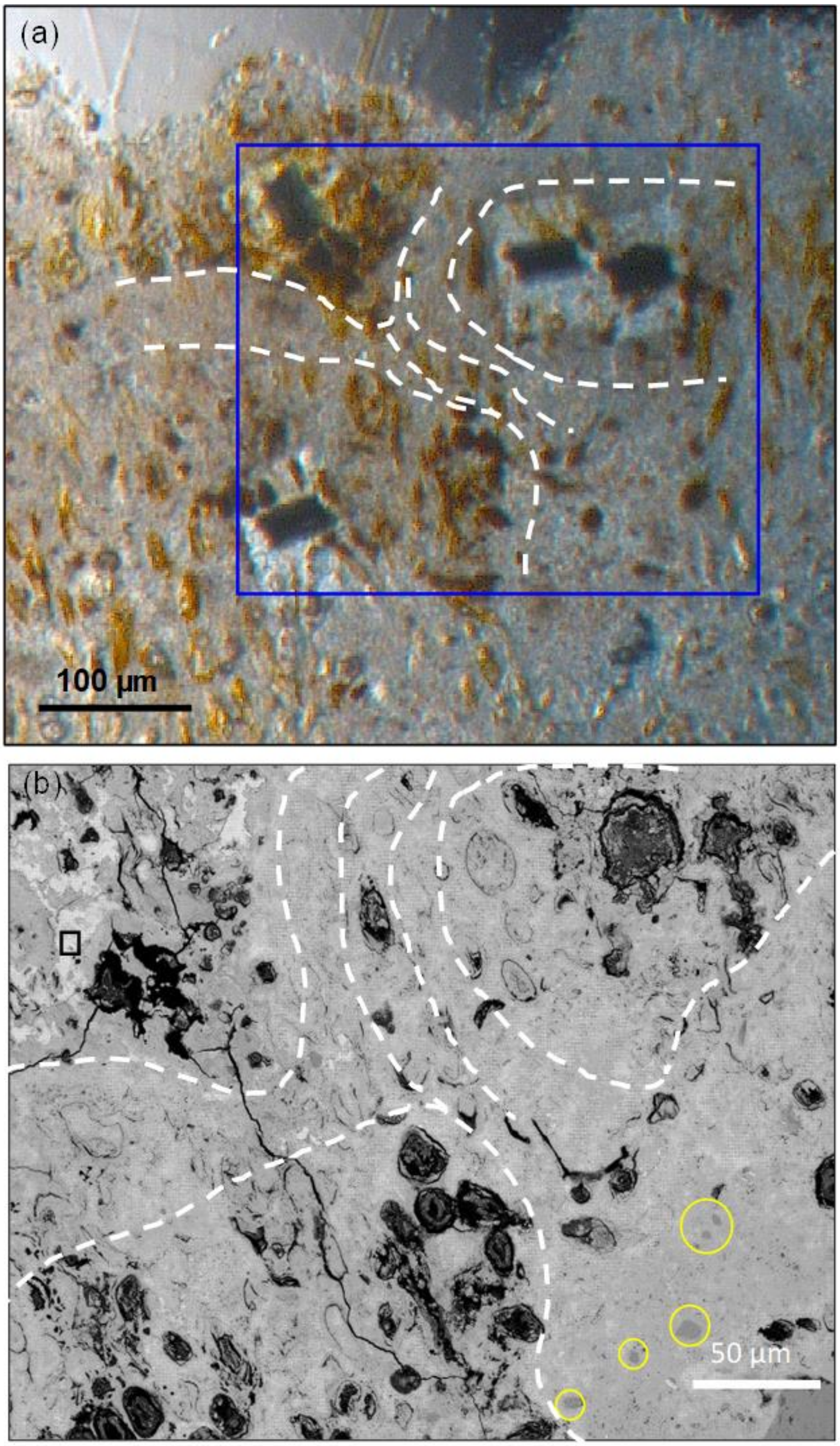

Fig. 6 Studied area corresponding to the yellow pin in Fig. 3b. The white dotted lines delimit the bright micro laminae full of microfossils from the dark micro laminae. (a): Optical image. The blue square delimit the area analyzed in (b). Note that the four dark squares correspond to excavations milled by FIB. (b) SEM-BSE micrograph. Contrast variations are indicative of chemical variations. Very bright areas (higher average atomic number) are observed in the top left-hand corner, whereas middle gray grains (lower average atomic number) are observed in the bottom right hand corner (yellow circle). The chemical composition of the bright area outlined by the black rectangle was analyzed in Table 3.

Table 3. Chemical composition of the whole EDX map and of the bright area in BSE (black square in Fig. 6.)

	Whole map		Bright area (square in Fig. 6)	
Element	**Mass [wt%]**	**abs. error [%] (2 sigma)**	**Mass [wt%]**	**abs. error [%] (2 sigma)**
Aluminium	0.96	0.01	0.08	0.03
Calcium	29	1.0	42	2
Carbon	12.3	0.1	9.8	0.1
Chlorine	0.12	0.02	0.21	0.04
Cobalt	1.6621	0.0007	/	/
Fluorine	1.08	0.02	/	/
Iron	1.62	0.04	/	/
Magnesium	3.10	0.03	0.27	0.03
Nitrogen	2.402	0.004	/	/
Oxygen	40.5	0.3	44.3	0.5
Potassium	0.151	0.006	1.1	0.3
Silicon	0.708	0.007	/	/
Sodium	0.615	0.008	0.80	0.03
Strontium	0.324	0.003	1.2	0.1
Sulfur	0.496	0.005	0.71	0.06
Mg/Ca (at)	**0.18**	0.02	**0.010**	0.003
Total	95		101	

Raw EDXS maps were converted into quantitative chemical maps (Fig. 7). The Mg/Ca ratio was evaluated to ~ 0.18 over the whole mapped area (Table 3), which is consistent with the values found by bulk analyses (Table 1). In agreement with µ-XRF analyses (Fig. 5) and the EDXS mosaic (Fig. S4), the Mg content reaches the highest values in the bright laminae. However, a Mg/Ca zoning can also be observed at a finer scale with a Mg enrichment around microfossils. Similarly, enrichments in Fe and F can also be seen around microfossils (Fig. S5). Several isolated submicrometer-sized grains, rich in Si are observed in the dark lamina in the bottom right hand corner of the maps (Fig. 7). Based on their Al, Na, or K contents, these grains are inferred to be clays and/or feldspar detrital grains as later discussed. Finally, microfossils and pores are well detected on the C map with some co-located enrichments with S, P, Al, Si, Co, N, Na and Cl. Nitrogen may be associated with indigeneous carbonaceous matter and/or amine groups composing the resin hardener (Fig. S5).

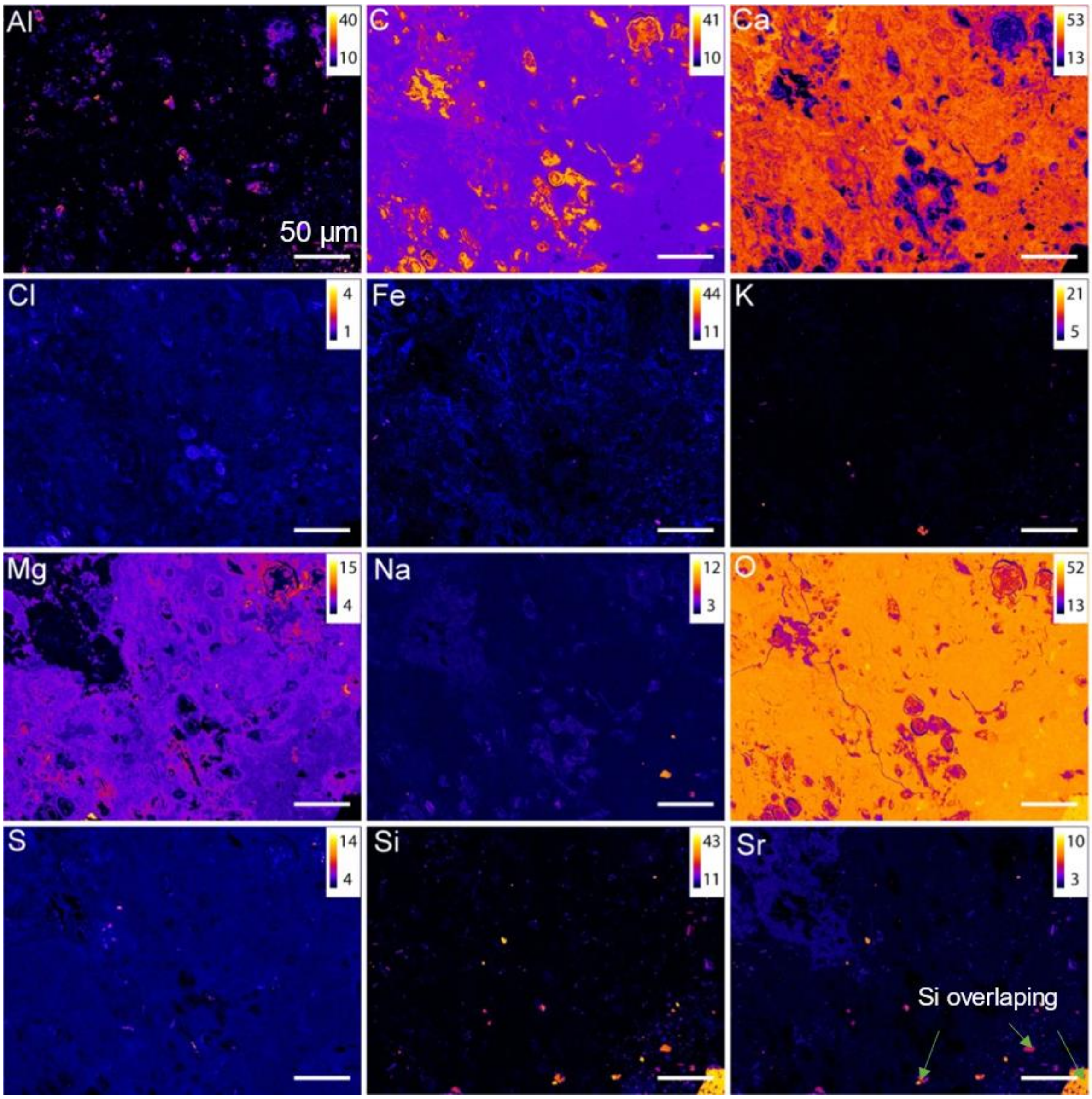

Fig. 7 Quantified SEM-EDXS maps of Al, C, Ca, Cl, Fe, K, Mg, Na, O, S, Si, Sr. Note that the green arrow indicates inaccurately quantified Sr hotspots due to an overlap between Si and Sr.

3.4. Deriving mineral phase maps and calculated mineral formulae of phases in the stromatolites from SEM-EDXS analyses

We obtained a mineral phase map based on the segmentation of pixels with similar chemical compositions using ternary scatterplot projections. Then, the mineral phase represented by these pixels is identified based on its stoichiometry (major and minor elements, including measured light elements such as O, F and C). For this purpose, pixel clusters are compared with the ideal composition of reference minerals. The mineral unit formula of the phase is latter refined based on the quantified EDXS analyses of a limited set of pixels recognized as representing a pure phase. The obtention of a fully equilibrated unit formula appears as a robust validation of the mineral identification. By contrast, mixtures appear as pixels aligned between clusters associated with pure mineral phases. Here, this approach was adapted to Mari Ermi stromatolites which contain numerous minerals with complex chemical compositions and extended solid solutions. Overall, it allowed to map the mineralogy of the samples with a few-hundreds-of-nanometer spatial resolution over an area measuring 10,000 square micrometers.

In order to distinguish the main types of phases in the mapped area, all pixels were first plotted in a 4(Al+Cl+P+S+Si)-C-O ternary diagram (Fig. 8a). Four main clusters were identified: (1) an organic-rich cluster corresponding to pixels with a high C/O ratio. When back-projected in the BSE image (Fig. 8b), their distribution is consistent with the darkest areas observed in BSE. Part of the porosity in the sample is filled by the resin used to prepare the petrographic thin sections. The other part of the porosity is filled by the remains of organic matter indigenous to the sample. Here, the term “organic-rich phase” encompasses both the carbon associated with the resin and the indigenous organic matter that cannot be properly distinguished from each other. Moreover, some remaining resin-free pores are encountered, and were segmented by an additional thresholding of the BSE image based on their low grey level values (removal of the darkest pixels). (2) A carbonate cluster was identified based on a C/(C+O) atom ratio of 0.75, perfectly matching their theoretical composition. This cluster was further analyzed by plotting the pixels in a 10Sr-Ca-Mg ternary plot (Fig. 9a).

We note that some, but not most of these segmented pixels consist of a mixture between carbonates and the “organic-rich phase”, but the latter was, by construction, limited in abundance in these pixels. In agreement with bulk analyses, carbonates are the most abundant phases since they show the maximum density in the scatterplot and were pervasive in the mapped area. (3) Finally, a so-called “non-carbonate” cluster was clearly evidenced. Its location in the ternary plot is slightly shifted towards carbon compared with pure quartz, talc or other silicate phases (Fig. 8a). This is due to the conductive carbon layer evaporated at the sample’s surface before SEM analyses. A few pixels (blue shade on the scatterplot corresponding to a local density lower than 100 pixels) trend towards the “organic-rich phase” cluster and the non-carbonate ones, corresponding to organic-rich phase mixed with the surrounding minerals.

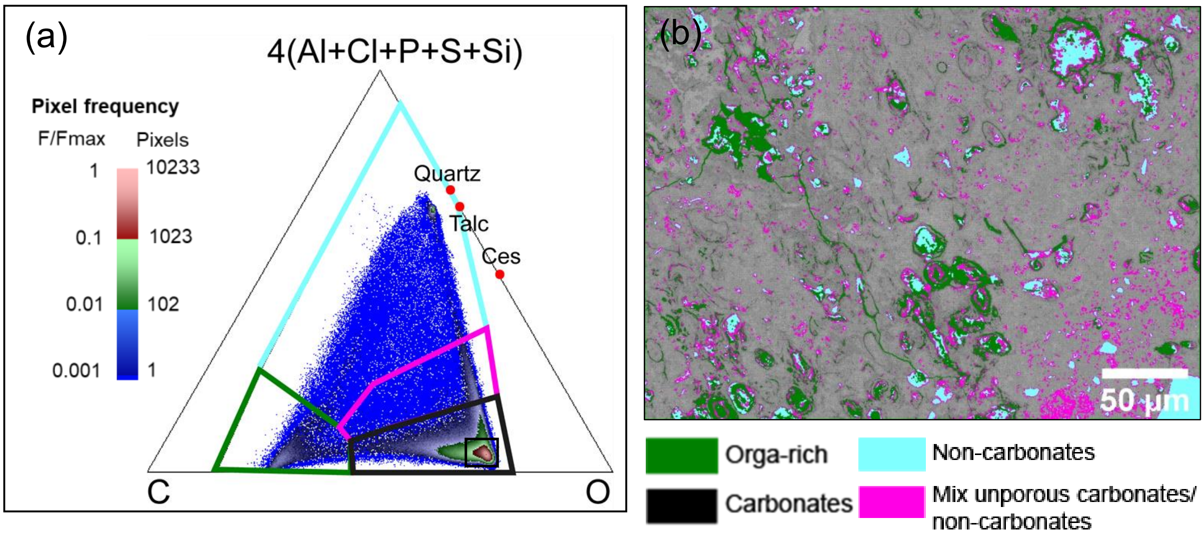

Fig. 8 Mineral phase mapping of organic-rich, carbonate, non-carbonate and carbonate/non-carbonate phases mixtures. (a) Plot of all the pixels of the mapped area in the 4(Al+Cl+P+S+Si) – C – O ternary diagram. Colored polygons outline the selected pixels for four clusters of mineral phases. Note the use of a logarithmic 3-band color scale which is indicative of the density of stacked pixels at each point of the ternary plot and allows to simultaneously represent poorly abundant compositions (in blue) and predominant compositions (in red). (b) Back-projection on a BSE image of the organic-rich (green), non-carbonate (cyan) and mixed carbonate-non-carbonate clusters (pink). Same color code as the polygons in the ternary. Carbonates are not back-projected since they compose most of the area.

The “non-carbonate” cluster is further divided in two subclusters after plotting pixels in a (Ca+K+Mg+Na+Sr)-3P-(Al+Si) diagram (Fig. 11a): one corresponds to apatite, gypsum, S-apatite and aluminum phosphate-sulfate (APS) phases and the other one to silicates, e.g., quartz, feldspar, and clay minerals (Fig. 13a). (4) A fourth cluster comprises pixels corresponding to an organic rich-phase/carbonates in mixture with non-carbonate phases (Fig. 8a). Carbonates are dominant in these mixtures and the non-carbonates grains are smaller than the X-ray emission volume. Even if they can be segmented separately in the same way than the "non-carbonate" cluster, the mixtures with carbonates drastically downgrade the clarity of the scatterplots presented hereafter. Therefore, the mineral phases comprised within these pixels were not retrieved and were not analysed further.

3.4.1. Segmentation of the carbonate cluster

The inclusive selection of pixels corresponding to carbonates in the 4(Al+Cl+P+S+Si) – C – O ternary diagram (Fig. 8a) was further analysed by plotting the corresponding pixels in a 10Sr-Ca-Mg ternary plot (Fig. 9a). This discriminated different carbonate phases, i.e. low magnesian calcite (Mg/Ca <0.05), high-magnesian calcite with a Mg-substitution (i.e., Mg/Ca) varying between 0.05 and 0.43, and a Sr-rich carbonate phase. Most pixels corresponding to magnesian calcite are aligned between pure calcite and dolomite (Fig. 9b). This shows that carbonate phases in Mari Ermi stromatolites belong to an extended solid solution between calcite and dolomite. There are no distinct clusters along this continuous solid solution and the highest pixel density corresponds to a Mg/Ca of 0.15, matching bulk estimations. The spatial distribution of Mg/Ca substitution was assessed by selecting four polygons along this mixing line corresponding to low magnesian calcite (LMC, Mg/Ca < 0.05), high magnesian calcite 1 (HMC 1, 0.05 < Mg/Ca < 0.18), high magnesian calcite 2 (HMC 2, 0.18 < Mg/Ca < 0.43) and very high magnesian calcite (VHMC, Mg/Ca > 0.43). Interestingly, HMC 2 and VHMC are systematically distributed around microfossils (Fig. 9b). By contrast, HMC 1 is distributed everywhere else. Only a few isolated grains of pure calcite are detected (LMC).

Few pixels showed a Mg/Ca higher than that of dolomite (Fig. 9a). This was surprising since there is a theoretical immiscibility gap for Mg above dolomite. One possible explanation is that these pixels correspond to a mixture between a carbonate phase and other Mg-rich phases. This hypothesis was confirmed by reprocessing the selection of the pixels in the 4(Al+Cl+P+S+Si) – C – O ternary diagram, choosing a more restrictive cluster (Fig. 8a) comprising only pixels corresponding to pure carbonate phases and excluding mixtures with other phases. When these pixels were replotted in the 10Sr-Ca-Mg ternary plot (Fig. S6a), only few pixels corresponding to VHMC were observed. However, this time, no dolomite cluster and no pixel with a Mg content higher than that of dolomite were detected (Fig. S6b). This suggests that there is no anomalous “Mg-too-rich” carbonate phase and that other Mg-bearing phases are mixed with carbonates in some pixels.

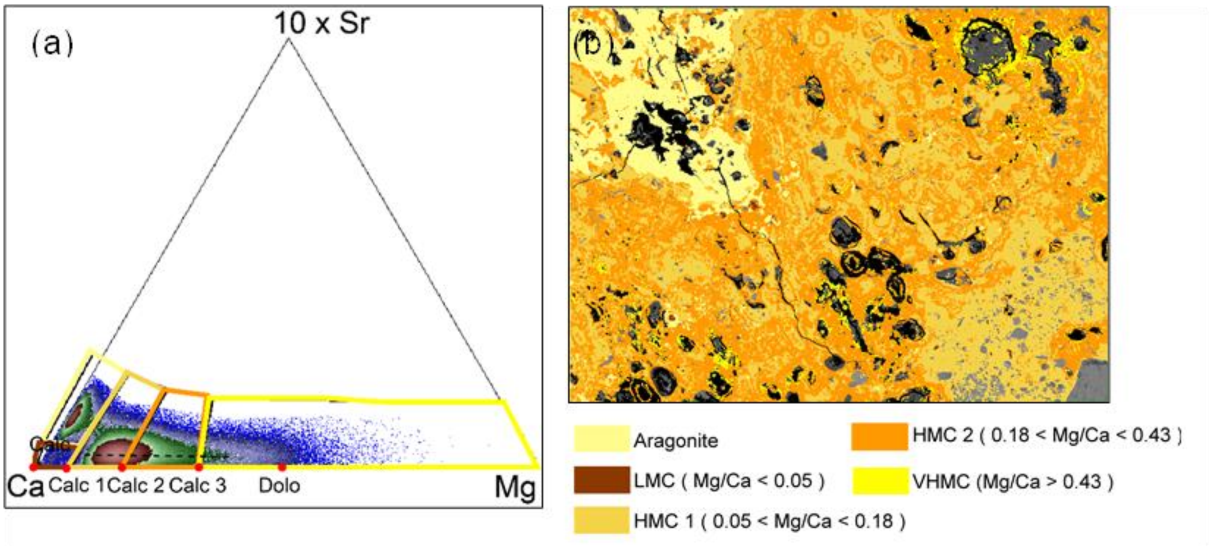

Fig. 9 Segmentation of the carbonate cluster. (a) The pixels corresponding to the carbonate cluster as defined in figure 8 are plotted in a 10Sr – Ca – Mg ternary diagram to discriminate five different carbonate phases. The dotted line highlights a solid solution between magnesian calcite (LMC) and very high magnesian calcite (VHMC). The red dots correspond to the theoretical chemical compositions implemented in the software µMAPphase (see Table S2) helping the segmentation of the low magnesian calcite (LMC), high magnesian calcite 1 (HMC), high magnesian calcite 2 (HMC 2) and very high magnesian calcite (VHMC) clusters.(b) The five different clusters of pixels are displayed on a mineral map and superimposed over the BSE image.

Some other pixels from the above-mentioned restrictive selection positioned along the Ca-Sr line in the 10Sr-Ca-Mg ternary plot, showing that some carbonates, not mixed with an “organic-rich phase” (hence non-porous), are enriched in Sr with no Mg. This suggests the presence of aragonite (Theye and Seidel, 1993). When back-projected on the BSE image, these pixels appear in the upper bright microlamina (Fig. 9b**)** over the intensely bright phase observed by BSE-SEM (Fig. 6). These non-porous carbonates are surrounded by similar porous (i.e., mixed with an “organic-rich phase”) Sr-rich carbonates (Fig. S6b**).** TEM-SAED of these Sr-bearing and Mg-poor carbonates analyzed in a FIB foil extracted from this area confirmed the presence of aragonite (Fig. 10). In addition, STEM-HAADF images confirmed that some aragonite was homogeneously bright, i.e. devoid of porosity, whereas some aragonite contained a lot of pores. We note that the presence of these pores does not prevent a robust determination of the calculated unit formula of these phases. Indeed, both porous and non-porous aragonites show similar Gaussian distributions for the frequency histograms of the number of Sr atom per formula unit, centered around 0.02 (Fig. S7, Table 4). Areas with a BSE brightness similar to the non-porous aragonite were rare but some could be observed in the large SEM mosaic (Fig. S2), in the upper part of the stromatolite only.

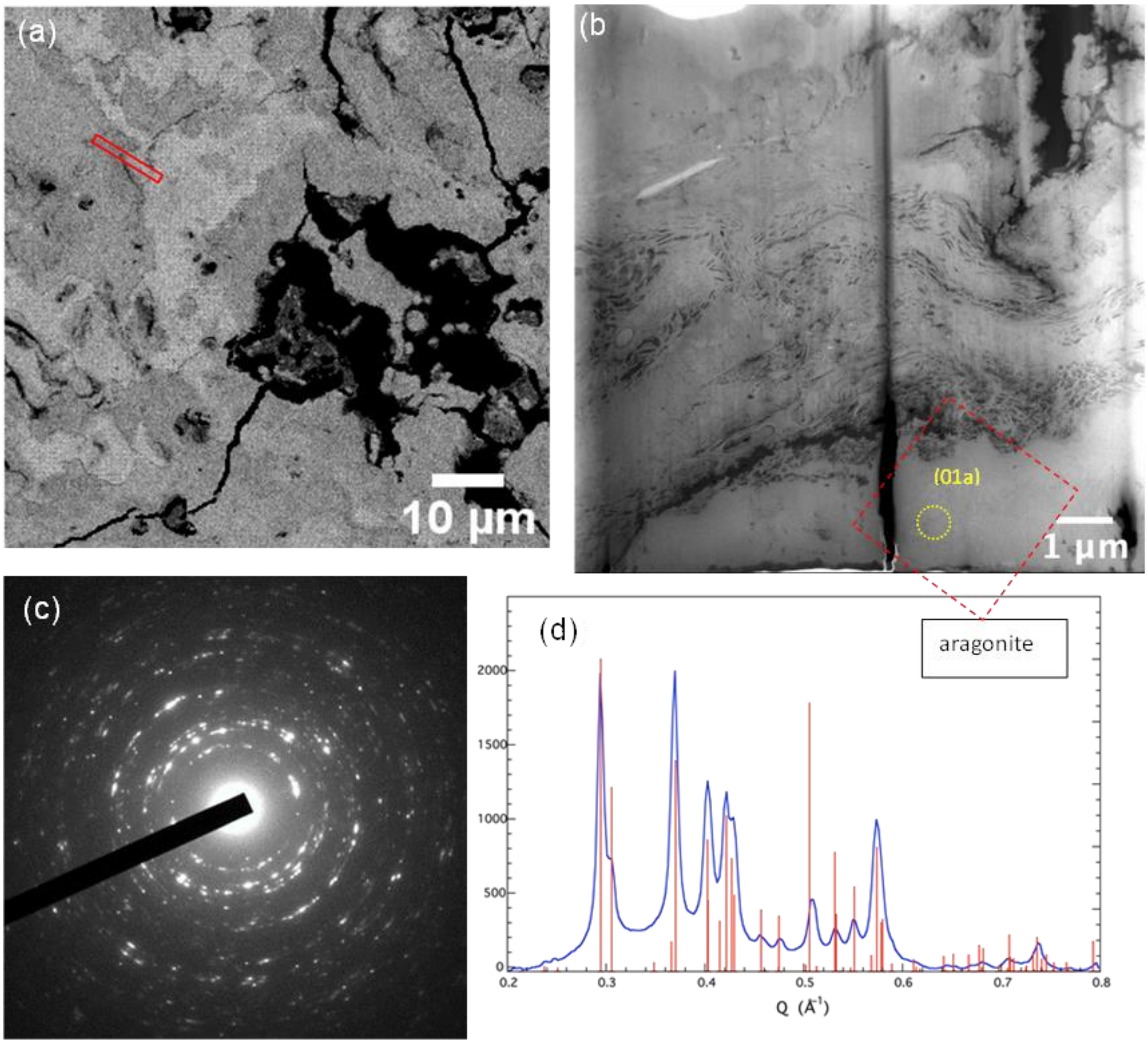

Fig. 10 Study of aragonite. (a) SEM image of the area where the FIB foil was extracted (b) STEM-HAADF image of the FIB foil extracted from the area outlined in (a). (c) Selected area electron diffraction pattern measured on the area labelled (01a) in (b). (d) Radial Fourier transform of the SAED pattern, indexed based on aragonite.

3.4.2. Segmentation of S- and P-bearing minerals

As mentioned above, the apatite was firstly discriminated by re-plotting pixels from the “non-carbonate” cluster in a (Ca+K+Mg+Na+Sr)-3P-(Al+Si) ternary plot (Fig. 11a). Some of the pixels in this diagram were scattered towards the P-apatite end-member ($Ca_5(PO_4)_3(F, OH, Cl)$). They were segmented as indicated in Figure 11a and back-projected on a map (Fig. 11b).

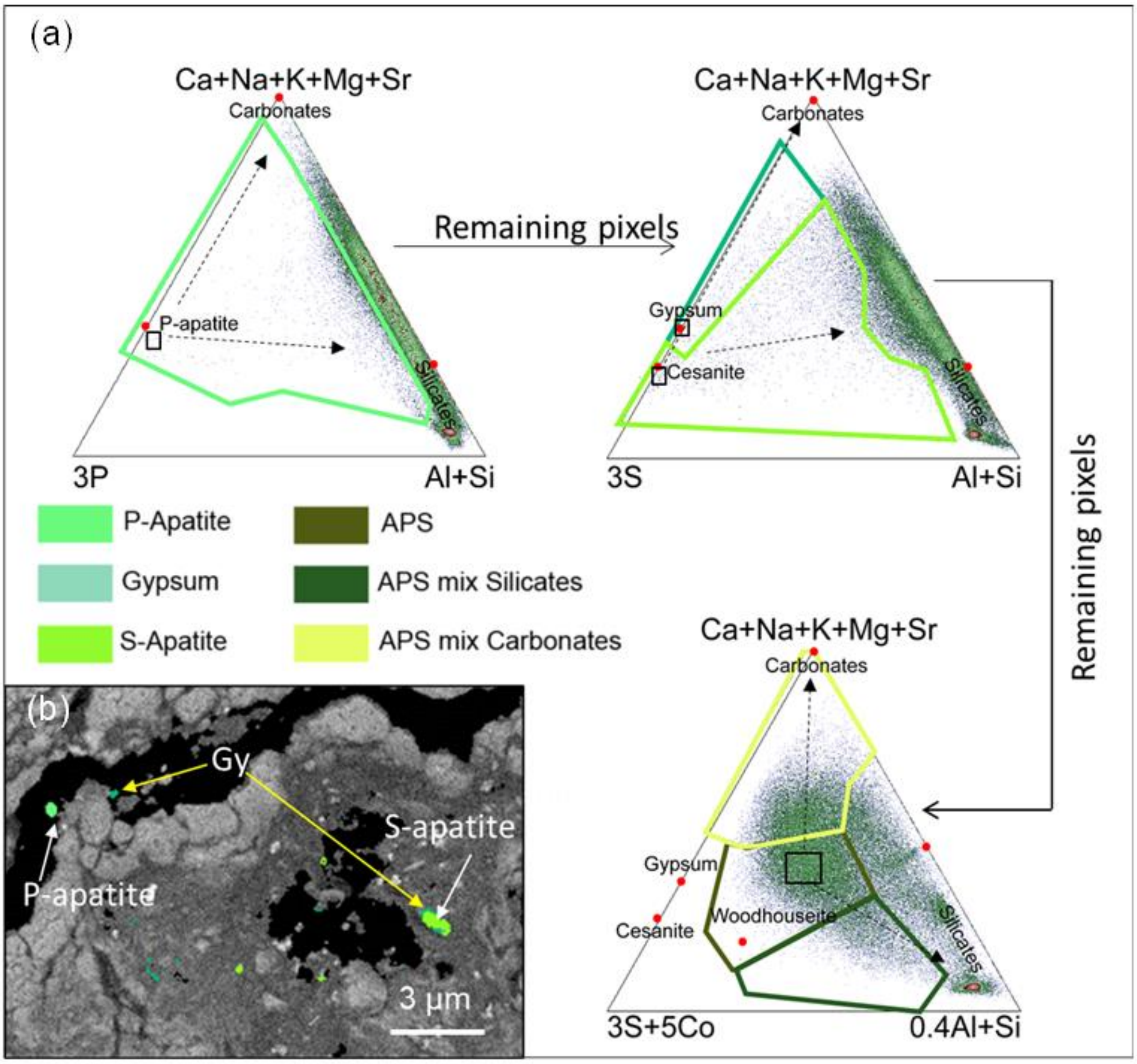

Fig. 11 Segmentation of the non-carbonate cluster (S- and P-bearing phases). (a) The cluster is first segmented in the Ca+Na+K+Mg+Sr-3P-Al+Si ternary plot. This evidences few pixels corresponding to P-apatite. The rest of the pixels are plotted in the Ca+Na+K+Mg+Sr-3S-Al+Si ternary plot which evidences pixels related to gypsum and S-apatite. The rest of the pixels are plotted in the Ca+Na+K+Mg+Sr-0.4Al+Si-Al+3S+Co ternary plot which evidences two clusters affiliated to S-apatite and gypsum. Their identification was confirmed by the determination of their average calculated unit formula (Table 4). (b) BSE image with the thresholded pixels. Note the possible overlap between gypsum and S apatite especially at the border of the grains (yellow arrow). The term APS refers to aluminum-phosphate-silicate phases that are speculated to be present but with no robust identification.

The remaining pixels were plotted in a (Ca+K+Mg+Na+Sr)-3S-(Al+Si) ternary plot (Fig. 11a). Some pixels were attributed to a gypsum-like phase ($CaSO_4,H_2O$). The term gypsum-like includes anhydrite, gypsum and any other Ca-sulfate phase with the same Ca/S stoichiometry but a different hydration level. Another group of pixels was attributed to S-apatite ($Ca_5(SO_4)_3$(F, OH, Cl)). S-apatites result from the substitution of PO_4 by SO_4 in an apatite structure. The distinction between S-apatite and gypsum-like phases was complicate because their theoretical endmembers were close to each other in terms of chemistry and they were both mixed with carbonates and silicates with some overlap of their mixture lines. The retrieval of two distinct mean mineral formulae from the purest pixels undoubtedly identified a gypsum-like phase with the following stoichiometry: $(Ca_{0.52}Na_{0.17}K_{0.05}Mg_{0.18}Co_{0.03}Si_{0.02}Al_{0.07})(C_{0.02}S_{0.98}O_4)(O_{0.89}F_{0.02},Cl_{0.03})$ and an S-apatite phase with the stoichiometry: $(Ca_{3.07}Na_{0.64}K_{0.17}Mg_{0.32}Fe_{0.02}Sr_{0.03}Co_{0.17})(P_{0.02}S_{1.86}Si_{0.16}Al_{0.33}C_{0.63}O_{12})(OH_{0.68},F_{0.22},Cl_{0.10})$. However, few gypsum-like pixels appeared within S-apatite grains after back-projection, suggesting also some overlapping mixture between both phases (Fig. 11b). TEM-SAED performed on a FIB foil extracted from this area showed the presence of γ -anhydrite (γ–$CaSO_4$, (Lager et al., 1984)) in agreement with the SEM identification of gypsum-like phases (Fig. 12). All the P and S-phases back-projected in the BSE image correspond to grains measuring few hundreds of nanometers in size (Fig. 11b). Furthermore, all these phases are located inside organic-rich microfossil areas. The remaining pixels (non-gypsum-like, non S-apatite) bearing S and Co were plotted in the (Ca+K+Mg+Na+Sr)-(3S+5Co)-(0.4Al+Si) ternary scatterplot (Fig. 11a). Even if no well-defined cluster was recognized, some pixels were distributed close to a solid solution between a Ca/Na/Sr-woodhouseite and a Al/Si-rich one and were tentatively attributed to "APS-like" mineral phases, the general mineral formula of which is $AB_3(XO_4)_2(OH)_6$, where A is a large cation (such as Na^+, K^+, NH_4^+, Ca^{2+}, Ba^{2+}, Sr^{2+}, REE), B may correspond to $Al^{3+,}$ Fe^{3+}, Cu^{2+} or Zn^{2+} and X is dominated by P and S (Dill, 2001). However, no mineral formula with an accurate charge balance could be retrieved so that the true nature of these pixels remains undetermined. Some other pixels were affiliated to a mixture between these undetermined "APS-like" phases and silicates or carbonates.

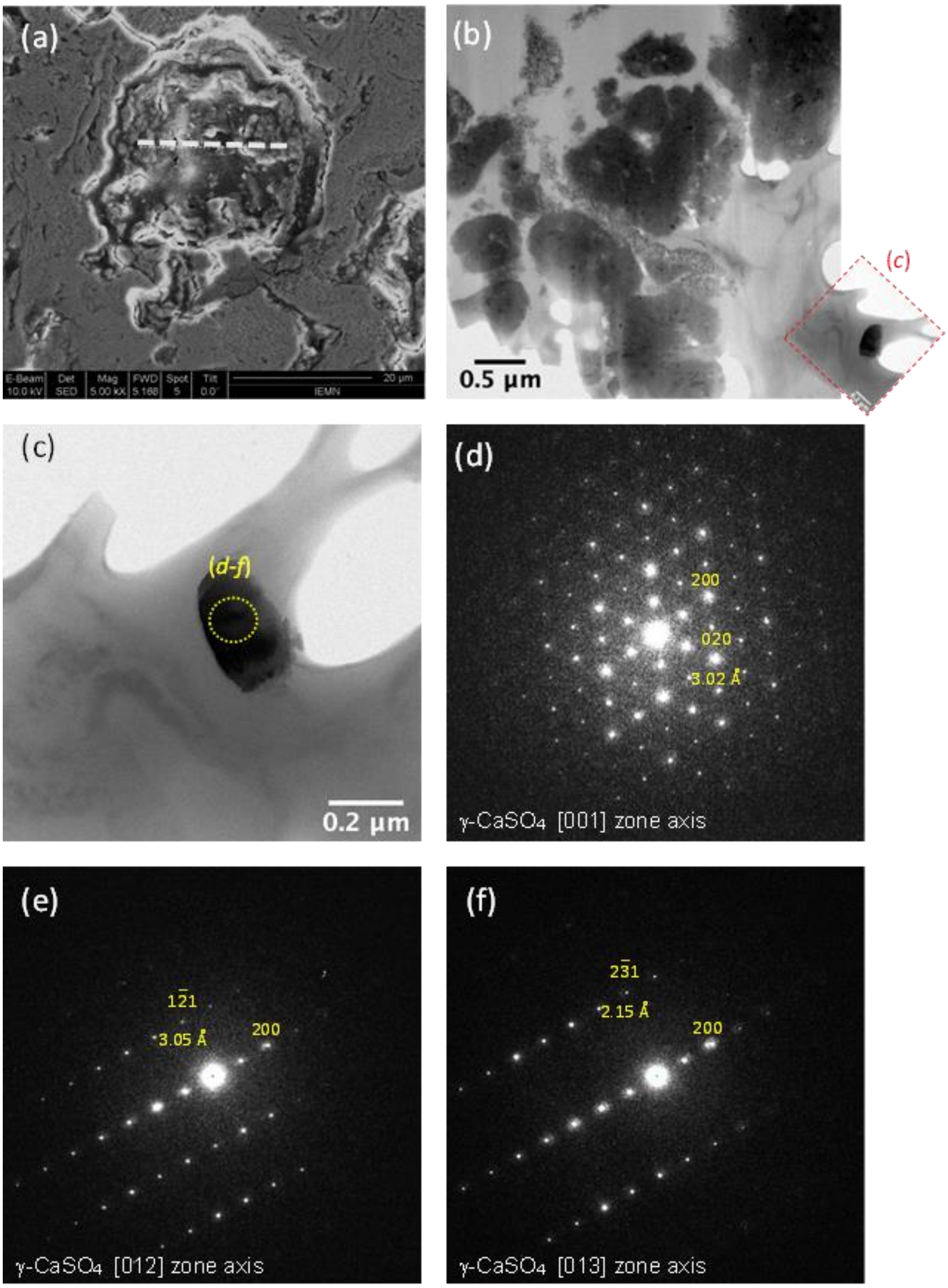

Fig. 12 TEM characterization of anhydrite (a) SEM image. The dashed white line outlines the location where the FIB foil was milled. (b) TEM bright-field image of part of the FIB foil. (C) Close-up of the area outlined in (b). The yellow circle outlines the area studied by SAED. (d-f) SAED patterns of the particle shown in (c) seen along different zone axes. They all match a γ-$CaSO_4$ (Lager et al., 1984)) structure observed along (d) [001], (e) [012] and (f) [013] zone axes.

3.4.3. Segmentation of quartz, feldspar, Al-phases and clay minerals

In order to segment the remaining pixels, they were plotted in a M-Si/4-2x(AlFeMg) ternary plot, where M = 2 x Ca (mol%) + Na (mol%) + K (mol%) (Fig. 13a). First, quartz grains and their mixture with carbonates and other silicates were segmented. Then, non-segmented pixels were plotted in a 2M–Si–2Al ternary diagram in order to discriminate Mg-rich silicates from Al-rich silicates, both mixed with carbonates (Fig. 13a). In this diagram, we could segment kaolinite in mixture with carbonates, and alkali feldspar (albite and orthose) also in mixture with carbonates (Fig. 13a). The pixels located along the 2 M – 2 Al axis correspond to Al-rich and Si-free phases. These Al nanograins may correspond to contaminants from the alumina suspension used for the preparation of petrographic thin sections.

Al-poor-Mg-rich silicates were detected, distributed close to the Si-2M axis along a mixture line. One endmember of this mixture line is centered on the theoretical composition of talc/kerolite/sepiolite/serpentine. Sepiolite and serpentine did not match with the measured chemical compositions as shown by projections in the M-Si/4-R2 ternary (Fig. S7a-b). Thus, this favors the presence of a talc-like phase (i.e., talc or kerolite). A more spatially resolved (pixel size of 61 nm) chemical map (Fig. 13b) was acquired in the area where talc-like phases were detected. It allowed to retrieve the following calculated mineral formula for the purest pixels: $(Ca_{0.01}Na_{0.08})(Si_{3.96}Al_{0.04})(Al_{0.03}Mg_{2.82}Fe_{0.09}Co_{0.01})O_{10}((OH_{1.37})F_{0.14}Cl_{0.01})$. Furthermore, TEM-SAED analyses of a FIB foil extracted from this area confirms the presence of a crystalline talc-like phase, i.e., talc or kerolite, which cannot be unambiguously distinguished from each other based on the available data (Fig. 14; Brindley et al., 1977).

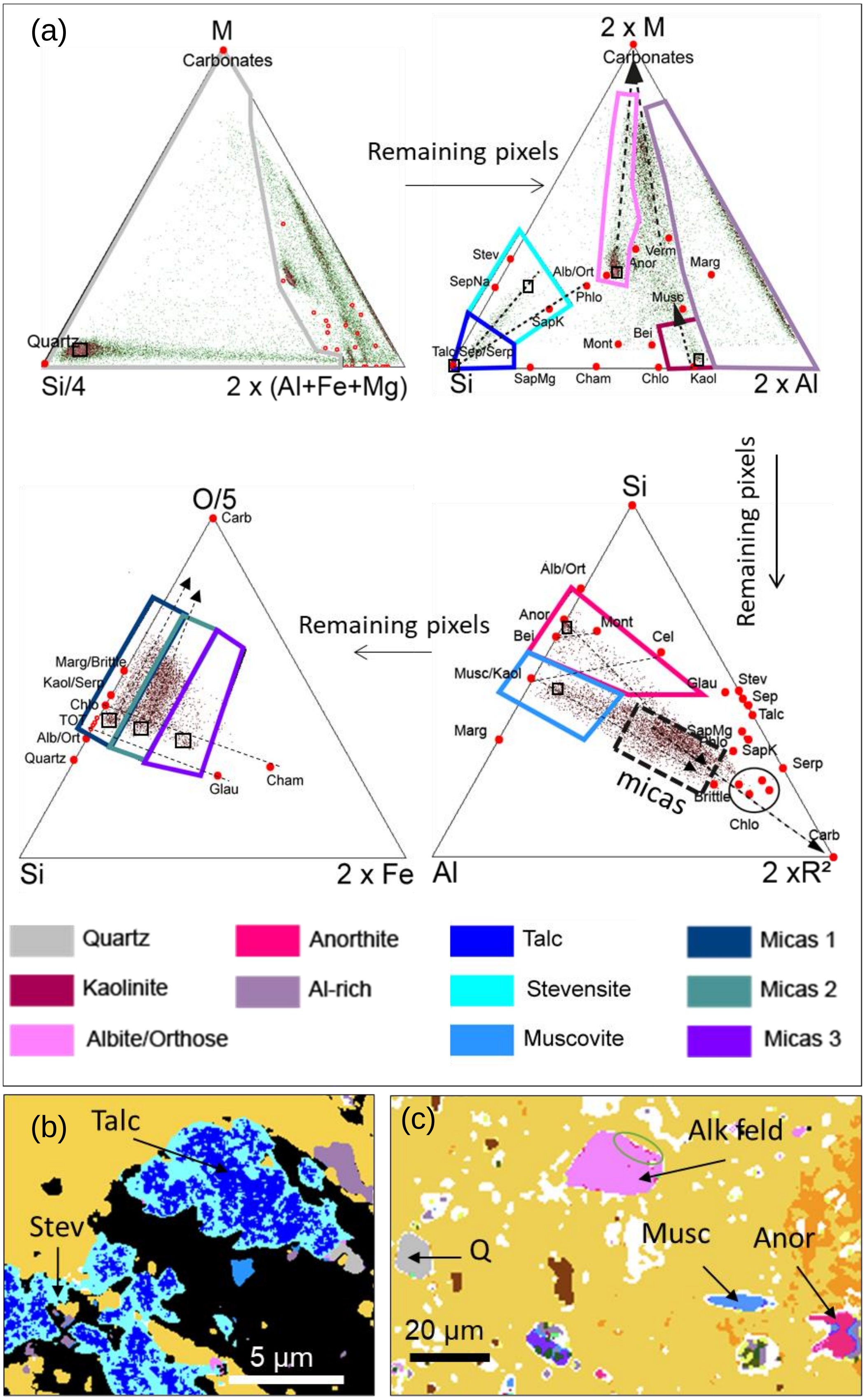
(a)
M
Carbonates
Quartz
Si/4
2 x (Al+Fe+Mg)
Remaining pixels
2 x M
Carbonates
Stev
SepNa
Alb/Ort
Phlo
SapK
Talc Sep/Serp
Verm
Anor
Marg
Musc
Bei
Mont
Si
SapMg
Cham
Chlo
Kaol
2 x Al
Remaining pixels
O/5
Carb
Marg/Brittle
Kaol/Serp
Chlo
TOT
Alb/Ort
Quartz
Glau
Cham
Si
2 x Fe
Remaining pixels
Si
Alb/Ort
Anor
Mont
Bei
Cel
Musc/Kaol
Glau
Stev
Sep
Talc
Marg
SapMg
Chlo
SapK
Serp
micas
Brittle
Chlo
Carb
Al
2 xR²
Quartz
Anorthite
Talc
Micas 1
Kaolinite
Al-rich
Stevensite
Micas 2
Albite/Orthose
Muscovite
Micas 3
(b)
Talc
Stev
5 µm
(c)
Alk feld
Q
Musc
Anor
20 µm

Fig. 13 Further segmentation of the non-carbonate cluster (silicate phases). (a) The pixels are first plotted in the M (2xCa+Na+K)-Si/4-2x(Al+Fe+Mg) ternary plot to segment quartz. The remaining pixels are plotted in the 2xM-Si-2xA ternary plot allowing to segment kaolinite, albite/orthose, talc and Al-rich phases. Non segmented pixels are plotted in the Si-Al-2 x R2 ternary plot, where R2 = Mg (mol%) + Fe (mol%). Last, the remaining pixels are plotted in the Si-O/5-2xFe ternary plot. This allows segmenting pixels affiliated to 3 different types of micas. TOT refers to the trioctahedral phyllosilicates = talc/sepiolite/kerolite/saponite/stevensite) (b) Mineral map calculated from a small hypermap (18 x 14 µm2, pixel size = 61 nm) centered around a talc-rich area. Note the presence of the talc-like phase (in blue) surrounded by a stevensite-like phase (Stev) in cyan. (c) Close-up of the alkali feldspar (Alk feld = orthose + albite), anorthite (Anor), muscovite (Musc) and quartz (Q) clusters back-projected on the BSE. Note the physical contacts between alkali feldspar and anorthite which explain the existence of mixing trends between these phases (green circle).

In the 2M–Si–2Al ternary diagram (Fig. 13a), pixels corresponding to the pure talc-like cluster stretch along a line. This can be explained by the fact that chemical compositions of clay minerals can be highly complex due to diverse extended solid solutions. When Al^{3+} substitutes a Si^{4+} in a tetrahedral sheet, this causes a charge deficiency in the T-O-T layer which is compensated by K^{+}, Ca^{2+} or Na^{+}, bonded in-between successive T-O-T layers as observed in saponite/phlogopite (or iron-rich glauconite). For trioctahedral phyllosilicates, the decrease of Mg^{2+} content (or Fe $^{2+}$) in the octahedral sheet, induces a similar increase of the layer charge as observed for stevensite. Consequently, the talc-like cluster stretch can be interpreted as a solid solution/mixture between talc and either (i) glauconite or (ii) a phase or a mixture of phases located in-between stevensite and saponite. In the Si-Al-R^2 ternary plot (where R^2 = Mg (mol%) + Fe (mol%), Fig. S6b), the above-mentioned cluster radiating from talc does not elongate towards glauconite. Therefore, a simple talc/glauconite mixture is unlikely. Furthermore, the retrieved calculated mineral formula is $(Na_{0.19}K_{0.99})$ $(Si_{2.98},Al_{1.02})$ $(Al_{1.80}Mg_{0.17}Fe_{0.10}Co_{0.01})$ $O_{10}((OH)_{1.43}\ F_{0.18}Cl_{0.01})$. The low iron content further confirms that it does not match with glauconite. However, the mineral formula suggests both a saponite-like feature (relatively high tetrahedral Al) and a stevensite-like feature (relatively lower Mg octahedral occupancy). Tetrahedral and octahedral charges are balanced by interlayer Ca and Na. When back-projected on the BSE image, this phase/mixture of phases surrounds the pure talc inner cores in some grains and it is associated to microfossils.

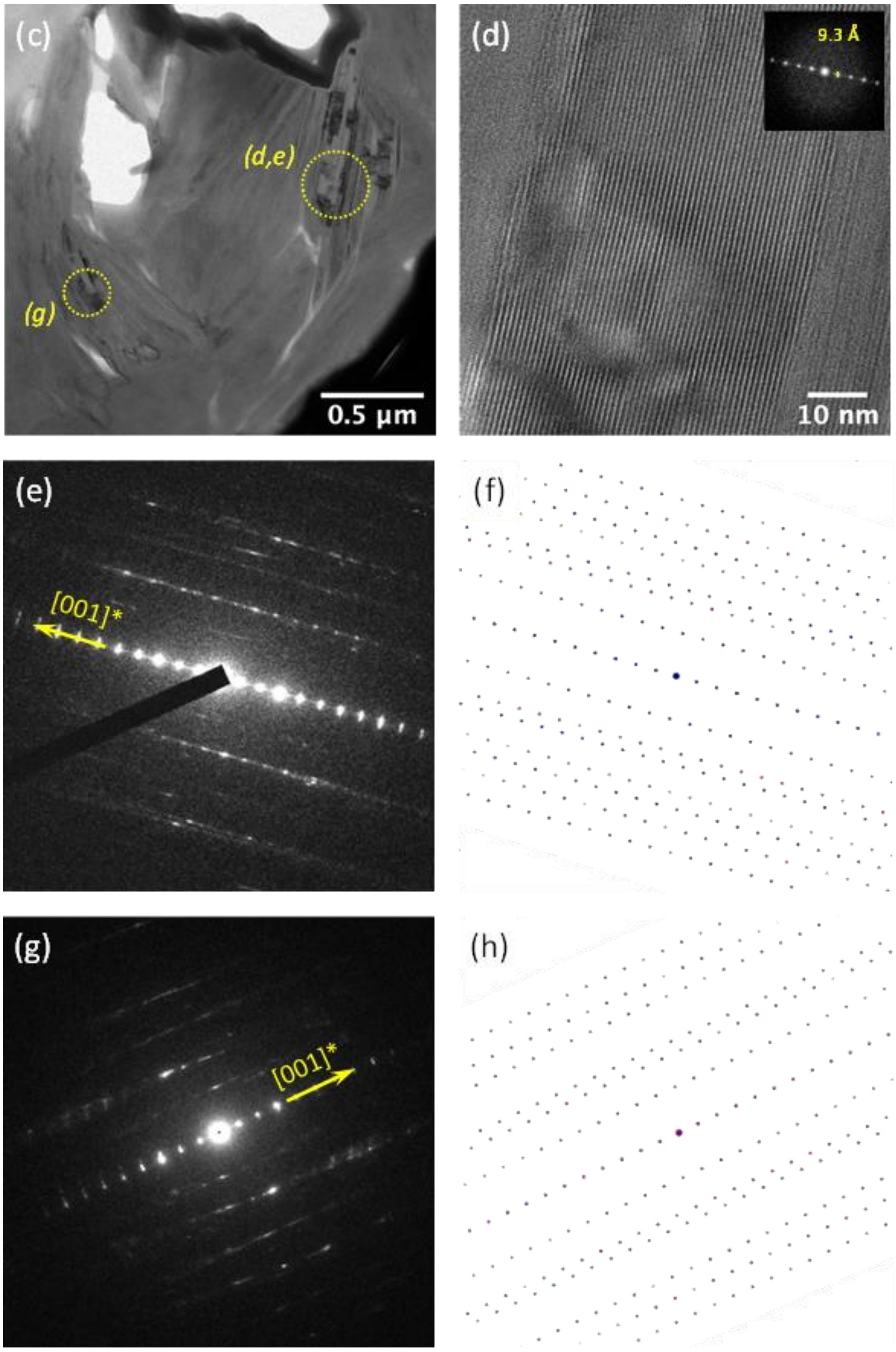

Fig. 14 Sudy of the talc-like phase (talc and/or kerolite). (a) SEM image showing the location from where the FIB foil was extracted (white dashed line). (b) STEM-HAADF image of the FIB foil extracted from the area outlined in (a). (c) Bright-field TEM close-up of the area outlined in (b), containing the talc-like phase. (d) HRTEM image showing the (001) planes of talc-like platelets. The insert shows the fast Fourier transform (FFT) pattern indicating a d-spacing equal to 9.3 Å. (e) SAED pattern related to the areas labelled (d,e) in image (c); (f) corresponding simulation calculated using a talc structure observed along [110]. (g) SAED pattern measured on the area labelled (g) in image (c); (h) corresponding simulation using a talc structure observed along [110] and [310] directions.

Last, pixels affiliated to anorthite are difficult to segment because their distribution overlaps that of pixels corresponding to mixtures between carbonates and other phyllosilicates located in the bottom part of the ternary plot (Fig. 13a). Among them, a cluster widely spread around the muscovite endmember is suspected. Overall, there are two remaining clusters of pixels: (i) one corresponds to anorthite and (ii) the other one to muscovite. Both are mixed with carbonates. The remaining pixels were plotted in a Si-Al-2R^2 ternary plot (Fig. 13a) in order to properly segment these two clusters. Anorthite and muscovite-containing pixels had the following calculated mineral formula for the purest pixels: $(Na_{0.76}Ca_{0.23}K_{0.03})(Si_{2.66}Al_{1.37})(O_{7.82},F_{0.05})$ and $(Ca_{0.15}Na_{0.18}K_{0.80})(Al_{1.05}Si_{2.95})(Al_{1.74}Mg_{0.17})O_{10}(OH_{1.97})$, respectively. Finally, several pixels plotted in the central part of the Si-Al-2R^2 ternary plot. They correspond to mixture lines between carbonates and both muscovite and anorthite but also another phase with a composition close to that of micas such as phlogopite or brittle micas. These remaining unidentified pixels in the micas area were plotted in an O/5-Si-2Fe ternary plot (Fig. 13a). Pixels scattered along mixing lines between carbonates and three clusters. All three clusters are close to the TOT – glauconite mixing line and beneath the chlorite-chamosite mixing line. No theoretical calculated mineral formula perfectly matched these three pixel-clusters. Overall, all pixels containing these diverse silicate phases were back-projected on the BSE image (Fig. 13c). They were distributed in the bottom right-hand corner dark lamina of Figure 6, which contains no microfossil (Fig. 6b**)**.

3.4.4. Summary mineralogical map and calculated mineral formulae

Overall, we computed a mineralogical map displaying the distribution of all the identified mineral phases (Fig. 15**)**, together with their associated calculated mineral formula and relative abundance (Table 4). With a mineral content of c.a. 80%, carbonates are the most abundant mineral phases, which was confirmed at a larger scale by bulk analyses. The mineralogical map highlights the remarkable distribution of the Mg/Ca ratio in calcite, with a higher Mg content within calcite around microfossils. The calculated mineral formulae for calcite show variations of the Mg/Ca from 0.02 in LMC up to 0.53 in VHMC. HMC 2 and VHMC are distributed in bright laminae and have an average Mg substitution of 0.21 and 0.53, respectively. With an average Mg/Ca of 0.15, HMC 1 is distributed in both bright and dark laminae. Some other phases such as (i) the Sr-rich carbonate, confirmed as aragonite owing to TEM-SAED, as well as (ii) clay minerals, are mostly distributed in dark laminae. The Sr/Ca in LMC, HMC 1 and HMC 2 is less than 0.2%, whereas it is more than 1% in aragonite. The mineral formula retrieved for carbonates with a C:O close to 1:3 confirms the good accuracy of the method for the determination of the calculated mineral formulae. The mineralogical map shows that P- and S-bearing phases measure few micrometers in size. They represent less than 0.5% of the mineral content. Their phases are borne by a small number of pixels, which make their identification difficult and they are distributed inside microporosities. Furthermore, they have a complex structure with various possible substitutions especially in apatite as shown here (Table 4) and in the literature (Nathan, 1984; McClellan and Van Kauwenbergh, 1990; Hughes and Rakovan, 2002; Pan and Fleet, 2002). Regarding silicate phases, quartz and feldspar are the most abundant ones and can reach centimeters in size. The determination of some phases remains uncertain: aluminum-phosphate-sulfate-like phases and micas. S-apatite is robustly supported by stoechiometric analyses. The identification of other phases is further supported by TEM data.

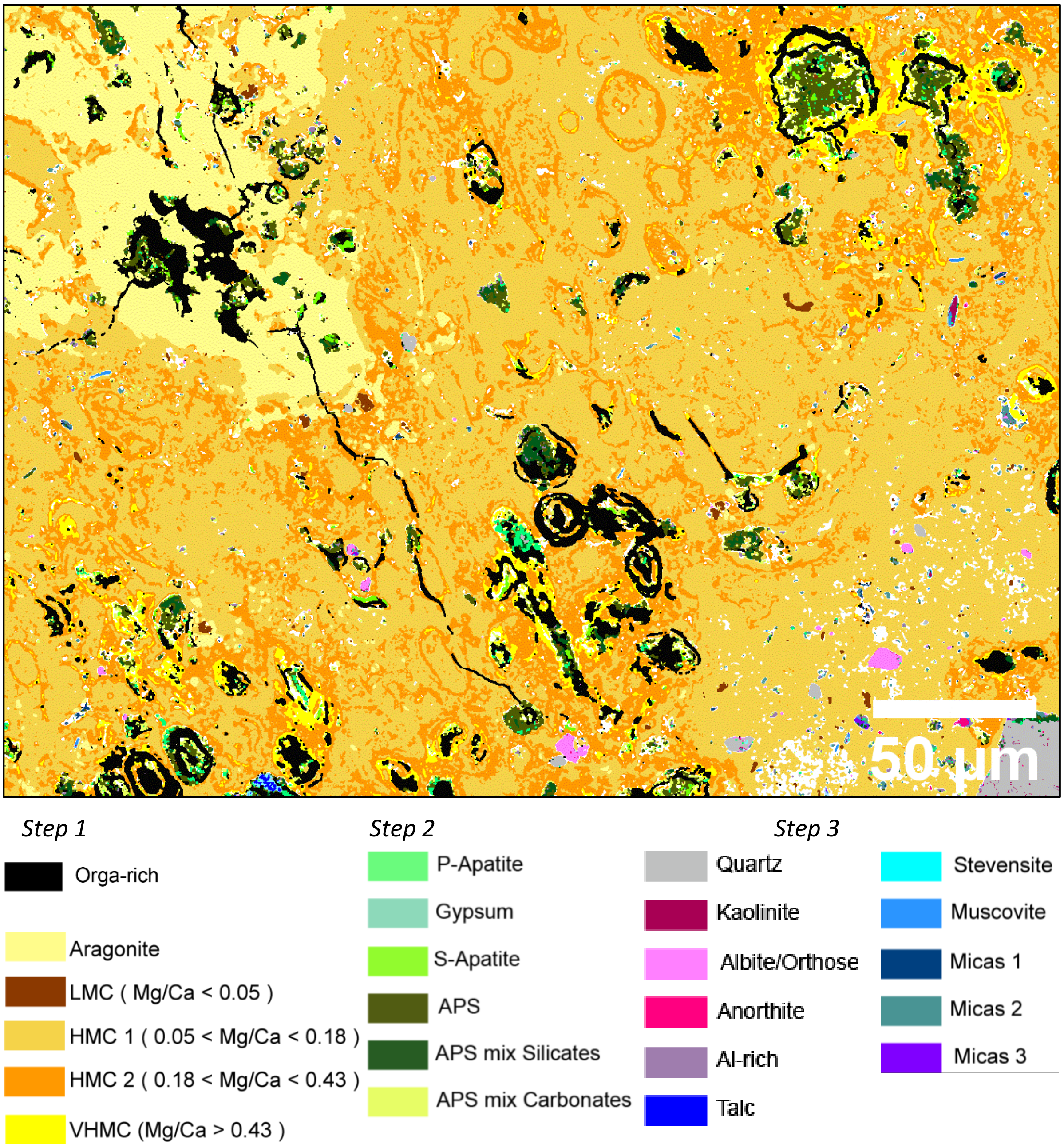

Fig. 15 Mineralogical map of the analyzed area of Mari Ermi stromatolite, obtained after successive segmentation steps (carbonates, and P-/S-baring phases and silicates/feldspar /clays). The white spots correspond to grains that were too small to be robustly segmented (e.g., mixtures between non-porous carbonates and non-carbonates phases in Fig. 8).

Table 4 Average calculated unit formula and mineral content of the mineral phases detected in Mari Ermi stromatolites and calculated from the SEM-EDXS hypermaps. Unit formulae have been calculated for a sum of 5 cations in the octahedron site for apatite; a sum of 1 cation in the calcium site for gypsum-like, and using a stoichiometric oxygen basis calculated from all the measured cations (including C for carbonates) for other minerals.

Mineral	Calculated stoichiometric formula	Mg/Ca	Mineral content (%)
Aragonite	$(Mg_{0.013}Sr_{0.014}Fe_{0.005}Ca_{0.97})C0_{.93}O_{2.8}F_{0.042}$	0.012	9
LMC	$(Mg_{0.022}Sr_{0.002}Fe_{0.009}Ca_{0.97})C0_{.98}O_{3.0}F_{0.042}$	0.023	0.2
HMC 1	$(Mg_{0.13}Sr_{0.003}Fe_{0.008}Ca_{0.86})C_{0.94}O_{2.9}F_{0.046}$	0.15	52
HMC 2	$(Mg_{0.19}Sr_{0.003}Fe_{0.01}Ca_{0.82})C_{0.94}O_{2.8}F_{0.057}$	0.21	21
VHMC	$(Mg_{0.34}Sr_{0.002}Fe_{0.02}Ca_{0.64})C_{0.97}O_{2.9}F_{0.066}$	0.53	3
P-apatite	$(Ca_{3.0}Na_{0.66}K_{0.10}Mg_{0.32}Fe_{0.09}Sr_{0.01}Si_{0.13}Al_{0.59})(P_{2.64}S_{0.13}Si_{0.01}O_4)(OH_{0.32},F_{0.55},Cl_{0.33})$		0.3
S-apatite	$(Ca_{3.07}Na_{0.64}K_{0.17}Mg_{0.32}Fe_{0.02}Sr_{0.03}Co_{0.17})(P_{0.02}S_{1.86}Si_{0.16}Al_{0.33}C_{0.63}O_{12})(OH_{0.68},F_{0.22},Cl_{0.10})$		0.2
Gypsum-like	$(Ca_{0.52}Na_{0.17}K_{0.05}Mg_{0.18}Co_{0.03}Si_{0.02}Al_{0.07})(C_{0.02}S_{0.98})(O_{4.89}F_{0.02},Cl_{0.03})$		0.04
Quartz	$Si_{0.95}O_{2.0}$		0.7
Kaolinite	$Al_{2.0}Si_{1.9}O_4(OH)_{3.8}$		0.03
Alkali feldpsar	$(Na_{0.85}K_{0.23}Ca_{0.01})(Si_{2.90}Al_{1.09})(O_{7.89,}F_{0.05})$		0.2
Anorthite	$(Na_{0.76}Ca_{0.23}K_{0.03})(Si_{2.66}Al_{1.37})(O_{7.82},F_{0.05})$		0.3
Talc-like	$(Ca_{0.01}Na_{0.08})\ (Si_{3.96}Al_{0.04})\ (Al_{0.03}Mg_{2.82}Fe_{0.09}Co_{0.01})\ O_{10}((OH_{1.37})F_{0.14}Cl_{0.01})$		0.02
Stevensite-like	$(Na_{0.19}K_{0.99})\ (Si_{2.98},Al_{1.02})\ (Al_{1.80}Mg_{0.17}Fe_{0.10}Co_{0.01})\ O_{10}((OH)_{1.43}\ F_{0.18}Cl_{0.01})$		0.02
Muscovite	$(Ca_{0.15}Na_{0.18}K_{0.80}(Al_{1.74}\ Mg_{0.17})(Si_{2.95}Al_{1.05})\ O_{10}(OH)_{1.97}$		0.05

4. Discussion

4.1. Mineralogy of carbonates and origin of the laminae in Mari Ermi stromatolites

X-ray diffraction, FTIR, µXRF, and SEM-EDXS analyses all consistently show that magnesian calcite is the main mineral phase composing Mari Ermi stromatolites. Moreover, FTIR analyses together with TEM-SAED analyses demonstrate the presence of aragonite in minor abundance. Aragonite appears as a Sr-enriched and Mg-poor carbonate phase arranged in fine layers within bright laminae, as attested SEM-EDXS analyses. The Sr/Ca ratio of these carbonates reached up to 1.4, compatible with the ratio measured for some aragonite occurrences reported in the literature (Siegel, 1960; Katz et al., 1972). Bulk analyses agree with spatially resolved analyses about an average Mg/Ca ratio of ~ 0.1 – 0.2 in calcite. This ratio is commonly found in high-Mg calcite, (Paquette and Reeder, 1990; Stanienda-Pilecki, 2018). However, at the micrometer scale, µXRF and SEM-EDXS analyses show that there is not just one single calcite phase in Mari Ermi stromatolites with one single Mg/Ca value but several carbonate phases instead, with varying Mg/Ca ratios. In particular, SEM-EDXS analyses show the presence of low-Mg calcite grains with a Mg/Ca lower than 0.05 on one hand, and on the other hand a solid solution of high-Mg calcite with a Mg/Ca ratio varying continuously from 0.05 to 0.43. Mg-Ca carbonates with varying Mg substitutions were also reported in single stromatolites from the hypersaline Lagoa Vermelha (Keim et al., 2020) and the soda lake Petukhovskoe (Samylina and Zaytseva, 2019). Lagoa Vermelha shares some environmental similarities with Mari Ermi, which may explain the variations in the Mg content of calcite as further discussed later: they are both shallow coastal ponds with seasonal salinity fluctuations between brackish and hypersaline conditions (Bahniuk et al., 2015a; Moreira et al., 2004; Spadafora et al., 2010; Van Lith et al., 2002; Vasconcelos and McKenzie, 1997). Interestingly, calcite phases with diverse Mg contents were not randomly distributed in Mari Ermi stromatolites. At a global scale, the SEM-EDXS mosaic as well as the µ-XRF maps highlight that the laminae distribution is correlated with the Mg/Ca variations: calcite in bright laminae has a Mg content higher than calcite in dark laminae. Two possible non-exclusive scenarios may explain the fluctuating Mg content observed in calcite in the Mari Ermi stromatolites.

4.1.1. 1st scenario: full abiotic control of the mineralogy of Mari Ermi stromatolites

A first “abiotic evaporitic” hypothesis suggests that variations of Mg/Ca in calcite result from the evaporitic context of Mari Ermi. Indeed, carbonate mineralogy and chemical composition have been shown to be primarily controlled by the Mg/Ca ratio of the aqueous solution in which they form (Müller et al., 1972). Moreover, it has been shown that upon net evaporation, the dissolved Mg/Ca of water in ponds increases because almost pure calcite precipitates first (Hardie and Eugster, 1970). With the increase of the dissolved Mg/Ca, precipitating calcite becomes increasingly enriched in Mg. When evaporation proceeds further, other mineral phases may start to precipitate. Their identity depends on the initial chemical composition of the ponds, especially the (Ca+Mg)/2*(HCO_3^-) ratio (Hardie and Eugster, 1970). If enough carbonates remain in solution, some other carbonate phases may precipitate such as aragonite, huntite or hydromagnesite (Zeyen et al., 2021). Aragonite precipitates at a relatively high aqueous Mg/Ca ratio (although it contains very little Mg) because it is not kinetically inhibited by the presence of Mg, whereas calcite is (Berner, 1975). Therefore, the identification of some Sr-bearing aragonite in dark laminae, where no or only few microfossils are observed, might be explained by a relatively higher aqueous Mg/Ca ratio at the time this phase precipitates. Consistently with this scenario, Carvalho et al. suggested that the co-occurrence of HMC and aragonite in Lagoa Vermelha stromatolites resulted from different seasonal conditions (Carvalho et al., 2018). In our study, the rare occurrence of aragonite suggests that when the dissolved Mg/Ca is high enough to be conducive to aragonite precipitation, only little bicarbonate is left in the solution and therefore only limited carbonate precipitation occurs before the precipitation of other salts. Furthermore, aragonite is only found in the upper layers of Mari Ermi stromatolites. This may be due to a poor preservation of aragonite and a diagenetic transformation of this phase over time. Starting from seawater, evaporation usually ends with the precipitation of sulfate phases before chlorides. Accordingly, anhydrite and halite were observed, which could be the last minerals forming in the evaporative sequence described by Hardie and Eugster (1970). While we suspect that halite grains observed in the µ-XRF analyses are not in place and may have been artefactually mobilized to the surface of the sample during sample preparation, we assume that anhydrite was in place. Since we did not detect major amounts of gypsum-like phases in the stromatolites, it is possible that (i) they precipitate at some stage but then dissolve back, once less saline conditions reappear in the next season and/or (ii) that microbialites do not grow or grow only little during the high salinity episodes when those phases precipitate. Overall, this first scenario follows the idea that mostly the geochemical conditions of the environment impact the mineralogy and chemical composition of the Mari Ermi stromatolites. And also, that the mineralogical composition of Mari Ermi stromatolites does not record exhaustively the full range of salinities encountered in the Mari Ermi ponds, i.e. records only to a limited extent the most advanced stages, when halite and gypsum precipitate. This hypothesis is also consistent with the experimental study by Ries et al. (Ries et al., 2008), who advocated for an "abiotic-like" mineralogical response of bacterial biofilms to altered seawater Mg/Ca ratios upon $CaCO_3$ mineralization. They concluded that biofilm carbonatogenesis operates more through alkalinization than a local change of the dissolved Mg/Ca ratio in their microenvironment.

4.1.2. 2nd scenario: biological control of the mineralogy of Mari Ermi stromatolites

The second hypothesis is that the high to very high enrichment of Mg in calcite is biologically driven. This is in line with several studies emphasizing the role of microorganisms in high-Mg calcite formation (Van Lith et al., 2003; Kaczmarek et al., 2017). In particular, the role of sulfate-reducing bacteria has been pointed out, possibly involving an increase of pH and sulfate removal (Van Lith et al., 2003; Vasconcelos et al., 2006; Spadafora et al., 2010). As revealed by SEM-EDXS analyses, the spatial distribution of the high Mg-calcite is strongly correlated with the distribution of microbial fossils.

In our study, variations of the Mg/Ca ratio of calcite distribute along a gradient around microfossils. We note that this spatial correlation between microbial fossils and high Mg-calcite was observed even within a single lamina. In other words, we not only evidence different Mg/Ca compositions between two laminae but we also detect calcite phases with very different Mg/Ca ratios close to each other. The ones with the highest Mg/Ca are associated with fossil microbes.

This supports the idea that Mg/Ca variations might be mostly due to the proximity of microorganisms and not the prevailing global aqueous conditions, since the impact of the latter would be expected to be observed at a larger scale only (e.g., between different laminae)..

Several studies, including some using cultivated strains have shown that some microorganisms promote the formation of carbonate phases with a Mg content higher than what would be expected from the dissolved Mg/Ca ratio of the solution (Van Lith et al., 2003; Stephenson et al., 2008; Zhang et al., 2015; Al Disi et al., 2017, 2019; Han et al., 2017). The exact mechanism of the modulation of carbonate Mg content and the formation of high-Mg calcite remains uncertain but all these studies agree on the crucial role of organic molecules such as those composing exopolymeric substances (EPS), polyacrylic and polyaspartic acids, peptides or other carboxylated organic acids (Raz et al., 2000; Wang et al., 2009; Zhang et al., 2015; Liu et al., 2020). Zhang et al., 2015 suggested that this catalytic effect may result from interactions between organic molecules and the surface of calcite which displace water molecules, limiting hydration of Mg^{2+} and thereby facilitate Mg^{2+} incorporation within the carbonate phase structure. Overall, what we see in Mari Ermi laminae might be a consequence of such a high Mg incorporation in carbonate phases catalysed by e.g., the sheath of cyanobacteria and leading to their permineralization. Whether only specific organic molecules excreted by specific bacteria may be more prone to induce this Mg enrichment will need to be assessed in the future. Here, the precise taxonomic affiliation of the microfossils around which Mg enrichment occurs could not be achieved. However, based on the morphology of some of these fossils, i.e. filaments measuring several micrometers in length and width, Saint Martin and Saint Martin, (2015) suggested that they might affiliate with *Scytonema*-like filaments, similar to the ones observed in surficial biofilms. Last, we also observe at a local scale that Mg enrichments correlate with Fe and F enrichments. While the creation of locally anoxic microenvironments may explain enrichments in Fe, the origin of F enrichment remains to be explained in the future.

A last possibility conciliating the two scenarios is that the microbially-mediated enrichment of calcites in Mg might be accentuated in evaporitic environments, i.e. physico-chemical conditions prevailing in Mari Ermi lagoons may be crucial so that biological factors promote high Mg-carbonates formation. This idea is in line with recent studies which are studying the influence of abiotic parameters (e.g. pH, temperature, Mg/Ca, salinity) on the precipitation of microbially mediated Mg-carbonates (Al Disi et al., 2019, 2021). For instance, in a sabkha environment, salinity, temperature, Mg/Ca (Al Disi et al., 2019) and carbonate supply (Al Disi et al., 2021) have a strong effect on bacterial activity, which in turn affect the incorporation of Mg within the calcite.

Overall, a general scenario for the laminae formation could be the following (Fig. 16): (1) a biofilm settles at the surface of Mari Ermi stromatolites in a solution with a chemical composition close to that of seawater. At times of elevated salinity and high Mg/Ca ratio, high-Mg calcite starts permineralizing cyanobacteria filamentous sheaths and some high Mg-calcite also possibly forms in decaying matrices of EPS. Meanwhile, because of extreme fluctuations and steep chemical gradients occurring within the microbial mats, Mg-calcite with a lower Mg/Ca also crystallizes. Then, upon evaporation and the increase of dissolved Mg/Ca and salinity, some aragonite form. When bicarbonates finally lack, sulfate phases start precipitating. With time and degradation of the EPS, the individual carbonate layers merge together and lithify according to the amalgamation process (A. M. Bahniuk et al., 2015b; Vasconcelos et al., 2014). With conditions becoming harsher, microbes become inactive and the stromatolite stops growing. Sulfates and halite may further precipitate but they partly dissolve in the next season when water is supplied again. However, 2) A new season favorable for precipitation starts over, but this time, because there is little biomass and/or a low dissolved Mg/Ca, dark laminae, which are thicker and denser with a Mg/Ca between 0.05 and 0.1, form. At this point, freshwater excursions (meteoric water and/or groundwater) could affect the balance of dissolved nutrients

(P, N) and/or trace metals (e.g., Zn, Mn), which may in turn impact the microbially mediated precipitation of Ca-phosphate and especially Mg-containing calcite phases.

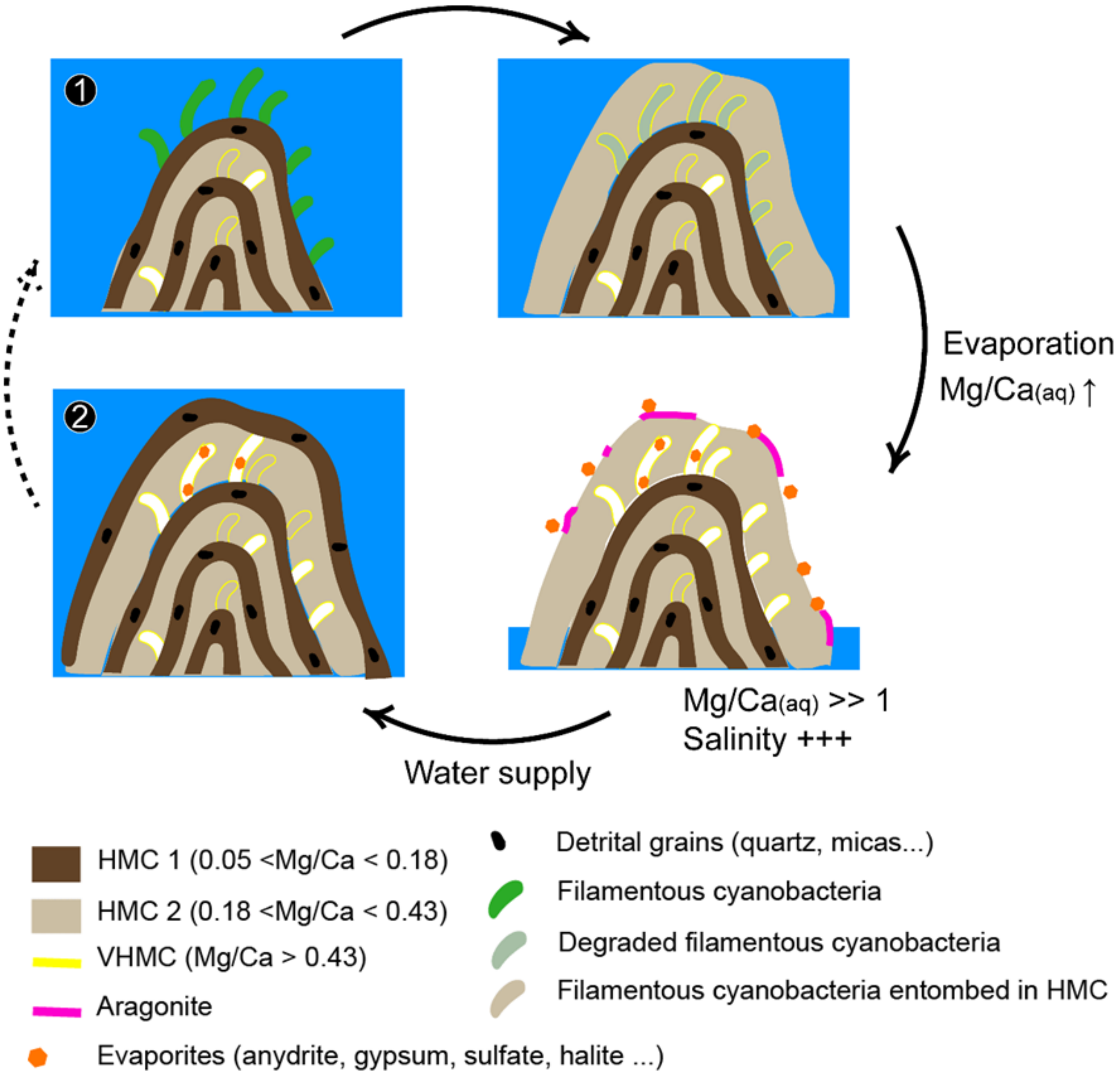

Fig. 16 Proposed sketch for the formation of Mari Ermi stromatolites over seasons. (1) Permineralization of the bacteria sheaths resulting in the formation of a bright lamina composed of HMC2 with a Mg/Ca higher than ~ 0.18. (2) Formation of a dark lamina composed of HMC1 with a Mg/Ca lower than 0.18. Note that no mineral phases related to Mari Ermi evaporation is recorded in the stromatolitic layers unless they are trapped and preserved in the microporosities.

4.2. Advantage of the quantitative SEM-EDXS approach: identifying possibly authigenic minor phases and their paleoenvironmental message

This study provides a clear example of the necessity to quantify and process EDXS analyses to retrieve the highest amount of mineralogical information in an heterogenous sample. First, quantifying EDXS hypermaps was essential to reliably assess the distribution of chemical elements in our samples. Indeed, whereas the raw EDXS maps of Ca and Mg (Fig. S9) suggested a quite homogeneous distribution, this was proved wrong by quantified maps which depicted a much more complex and informative pattern, with Mg enrichment of calcite around microfossils as discussed above. Then, although the BSE mosaic (Fig. S2) and BSE micrographs (Fig. 6) provide a slightly better spatial resolution than EDXS maps and are faster to acquire, contrast variations between some of the mineral phases are not high enough to clearly differentiate them, whereas they can be detected by quantified EDXS mapping.

Because the capability to identify the smallest grains requires to achieve the smallest beam interaction volume as possible, we used the lowest voltage that allowed exciting the X-ray emission lines of all chemical elements of interest. While bulk analyses such as FTIR and XRD detected only few mineral phases in Mari Ermi stromatolites, quantified SEM-EDXS maps at high spatial resolution allowed the detection of many more “minor” phases, both allochthonous and authigenic. As discussed below, the latter phases may provide clues about the geochemical and possibly biological conditions controlling their formation.

A first class of mineral phases undetected by bulk analyses but evidenced by SEM analyses was clay minerals. We advocate that some of these clays are authigenic, i.e. formed by direct precipitation from an aqueous solution (neoformed), or resulting from the transformation of a precursor (such as e.g. a detrital clay). Authigenic clays are particularly interesting since they have been shown to provide insight into the chemistry of the water in which they form/transform. Here, we detected some Al-poor and Mg-rich phyllosilicates by SEM-EDXS. They chemically resemble the amorphous Mg-phyllosilicates that have been increasingly found in modern carbonate microbialites (Zeyen et al., 2015; Chagas et al., 2016) and that precipitate spontaneously from alkaline, Mg- and H_4SiO_4-rich solutions (Birsoy, 2002; Tosca et al., 2011; Tosca and Masterson, 2014) Considering the low concentration of dissolved H_4SiO_4 in Mari Ermi water (Table S5), compared with other Mg-silicate-forming environments (Zeyen et al., 2015), we assume that Si may be provided by diatoms, which are abundantly found in this ecosystem (Saint Martin and Saint Martin, 2015). We note that in Mari Ermi they appear crystalline as attested by TEM-SAED on the contrary to many amorphous occurrences reported in freshwater systems. This might be due to a higher degree of dehydration (Tosca and

Masterson, 2014), resulting from the particular environmental conditions at Mari Ermi. In Mari Ermi, these phyllosilicates are detected in association with the “organic-rich phase” cluster suggesting a possible intimate association of these mineral phases with organic matter, if the latter is not just resin. Similarly, past studies reporting these phases evidenced their frequent association with organic molecules, especially extracellular polymeric substance (EPS) that may favour their precipitation (Konhauser and Urrutia, 1999; Souza-Egipsy et al., 2005; Perri et al., 2017; del Buey et al., 2018, 2021; Pace et al., 2018). It has been shown that the nature of the Mg-phyllosilicate phase that is precipitated (i.e. sepiolite, stevensite, talc or kerolite) depends on the prevailing environmental conditions, especially salinity (Decarreau, 1980; Kloprogge, 1999; Pozo, 2000; Tosca and Masterson, 2014). In Mari Ermi, TEM SAED and SEM-EDXS indicate that this phase was a talc-like phase (talc or kerolite). Moreover, EDXS data suggest the presence of a zoning with a talc-like phase in the center and stevensite which shows Al-enrichment (saponite like) in the outer part. According to Tosca and Masterson, (2014), stevensite preferentially forms in seawater at a high Mg/Si ratio (Mg/Si > 6) and at pH around 9 which is compatible with the conditions prevailing in Mari Ermi (Table S5) but the evolution detected from talc-like inner cores towards stevensite/saponite in the outer part will need further studies to be associated with the geochemical evolution of Mari Ermi solution.

Another example of mineral phases undetected by bulk analyses but evidenced by quantitative SEM-EDXS analyses are the P- and S-bearing phases. P-bearing phases usually consist of P-apatite, which is widely found in nature and have lately been increasingly reported in carbonate deposits/microbialites from alkaline lakes (Zeyen et al., 2021; Pietzsch et al., 2022). Some F and Cl enrichment was detected in P-apatite, consistent with the presence of chlor- and fluoro-apatite. In Mari Ermi stromatolites, P-apatite phases may result from the diagenetic decomposition of P-containing organic matter and the diversion of part of the released orthophosphate anions to apatite precipitation favored by the high Ca concentration in seawater (Baturin, 1982, 1988). Alternatively, they may form authigenically with relatively high dissolved orthophosphate concentrations possibly favored by evaporation and high alkalinity as suggested by Pietzsch et al. (2022).

S-bearing phases encompass gypsum ($CaSO_4 . 2H_2O$), corresponding dehydrated phases (basanite, anhydrite) and S-apatite (e.g., cesanite, $Ca_2Na_3[(OH)(SO_4)_3]$). Anhydrite in Mari Ermi stromatolites is interpreted as an evaporitic byproduct as mentioned above. The well equilibrated unit formula highlights strong substitution of Ca by Na, Mg, Al. More surprisingly, we also clearly detect S-bearing phases which differ from gypsum based on their stoichiometry and are affiliated to S-apatite. Compared to apatite, the substitution of PO_4^{3-} by SO_4^{2-} in S-apatite results in a negative charge deficit, which is compensated by an increase of Na^+ and K^+ substituting calcium. Here, some substitutions of S by Si/Al and Ca by Co are detected when retrieving the unit formulae. S-apatite also contained Cl and F similarly to P-apatite. Unfortunately due to their very small size, these particles could not be successfully retrieved by FIB for further TEM analyses. To our knowledge, S-apatites have not been reported in microbialites before. Interestingly, some occurrences of these phases have been reported in low-temperature systems, especially in caves (Onac et al., 2001). In these cases, cesanite was associated with hydroxylapatite and filled corroded pits in gypsum. It was suggested to precipitate directly from a sodium- and sulfate-rich, calcium-depleted solution, possibly following gypsum precipitation (Onac and Vereş, 2003). Overall, S-apatite may speculatively be either seen as an alteration product of apatite and/or gypsum by a Na- and SO_4-rich solution such as that found in Mari Ermi lagoon, or appear as one intermediate of the evaporitic sequence precipitating when Ca becomes depleted relatively to sulfates. Investigating the solubility of cesanite formed at low temperature, will help in the future to constrain the Ca, Na, SO_4^{2-} concentrations and pH necessary for its formation which may therefore allow its use as a paleoenvironmental proxy.

Acknowledgements

We would like to thank the financial support from the Paris Ile-de-France Region – DIM "Matériaux anciens et patrimoniaux" (MAP). We also thank financial support from the French national INSU program Interrvie. KB is funded by the French Agence Nationale de la Recherche (ANR), under grant Microbialite, ANR-18-CE0-0013-02. We would also like to thank several instrumentation facilities located at IMPMC that enabled streamlines measurement and analysis of datasets presented in this work: Maxime Guillaumet and Keevin Béneut for the Spectroscopy platform; Imène Esteve, Stéphanie Delbrel and Béatrice Doisneau for SEM support; Ludovic Delbes and Benoît Baptiste for X-ray diffraction facility and Jean Michel Guignier for TEM platform. We thank SARM (Nancy, France) for bulk chemical analyses. We thank David Troadec from IEMN for the FIB sections preparation. We thank France Lam for macro-apotome imaging. We thank Laurane Fogret and Stefan Lalonde for µ-XRF analyses. We thank Simona Saint Martin for her proofreading of the manuscript. We thank

Samuel Domino for bulk analyses. We thank Margot Coutaud and Laure Cordier for wet chemical analyses. Last, we thank Massimo Marras and Roberto Brundu and at a larger scale all the staff from the marine protected area "Peninsula of Sinis - Island of Mal di Ventre".

References

Al Disi, Z. A., Bontognali, T. R. R., Jaoua, S., Attia, E., Al-Kuwari, H. A. S., and Zouari, N. (2019). Influence of temperature, salinity and Mg 2+ :Ca 2+ ratio on microbially-mediated formation of Mg-rich carbonates by Virgibacillus strains isolated from a sabkha environment. *Scientific Reports* 9, 19633. doi: 10.1038/s41598-019-56144-0.

Al Disi, Z. A., Jaoua, S., Bontognali, T. R. R., Attia, E. S. M., Al-Kuwari, H. A. A. S., and Zouari, N. (2017). Evidence of a Role for Aerobic Bacteria in High Magnesium Carbonate Formation in the Evaporitic Environment of Dohat Faishakh Sabkha in Qatar. *Front. Environ. Sci.* 5. doi: 10.3389/fenvs.2017.00001.

Al Disi, Z. A., Zouari, N., Attia, E., Al-Asali, M., Al Saad Al-Kuwari, H., Sadooni, F., et al. (2021). Systematic laboratory approach to produce Mg-rich carbonates at low temperature. *RSC Adv.* 11, 37029–37039. doi: 10.1039/D1RA06206A.

Bahniuk, A. M., Anjos, S., França, A. B., Matsuda, N., Eiler, J., Mckenzie, J. A., et al. (2015a). Development of microbial carbonates in the Lower Cretaceous Codó Formation (north-east Brazil): Implications for interpretation of microbialite facies associations and palaeoenvironmental conditions. *Sedimentology* 62, 155–181. doi: 10.1111/sed.12144.

Bahniuk, A., McKenzie, J. A., Perri, E., Bontognali, T. R. R., Vögeli, N., Rezende, C. E., et al. (2015b). Characterization of environmental conditions during microbial Mg-carbonate precipitation and early diagenetic dolomite crust formation: Brejo do Espinho, Rio de Janeiro, Brazil. *Geological Society, London, Special Publications* 418, 243–259. doi: 10.1144/SP418.11.

Baturin, G. N. (1982). *Phosphorites on the sea floor*. Elsevier.

Baturin, G. N. (1988). Disseminated phosphorus in oceanic sediments — A review. *Marine Geology* 84, 95–104. doi: 10.1016/0025-3227(88)90127-2.

Benzerara, K., Menguy, N., Guyot, F., Vanni, C., and Gillet, P. (2005). TEM study of a silicate-carbonate-microbe interface prepared by focused ion beam milling. *Geochimica et Cosmochimica Acta* 69, 1413–1422. doi: 10.1016/j.gca.2004.09.008.

Berner, R. A. (1975). The role of magnesium in the crystal growth of calcite and aragonite from sea water. *Geochimica et Cosmochimica Acta* 39, 489. doi: 10.1016/0016-7037(75)90102-7.

Birsoy, R. (2002). Formation of sepiolite-palygorskite and related minerals from solution. *Clays and Clay Minerals* 50, 736–745. doi: 10.1346/000986002762090263.

Brindley, G. W., Bish, D. L., and Wan, H.-M. (1977). The nature of kerolite, its relation to talc and stevensite. *Mineral. mag.* 41, 443–452. doi: 10.1180/minmag.1977.041.320.04.

Carvalho, C., Oliveira, M. I. N., Macario, K., Guimarães, R. B., Keim, C. N., Sabadini-Santos, E., et al. (2018). Stromatolite Growth in Lagoa Vermelha, Southeastern Coast of Brazil: Evidence of Environmental Changes. *Radiocarbon* 60, 383–393. doi: 10.1017/RDC.2017.126.

Chagas, A. A. P., Webb, G. E., Burne, R. V., and Southam, G. (2016). Modern lacustrine microbialites: Towards a synthesis of aqueous and carbonate geochemistry and mineralogy. *Earth-Science Reviews* 162, 338–363. doi: 10.1016/j.earscirev.2016.09.012.

Decarreau, A. (1980). Cristallogenèse expérimentale des smectites magnésiennes : hectorite, stévensite. *bulmi* 103, 579–590. doi: 10.3406/bulmi.1980.7423.

del Buey, P., Cabestrero, Ó., Arroyo, X., and Sanz-Montero, M. E. (2018). Microbially induced palygorskite-sepiolite authigenesis in modern hypersaline lakes (Central Spain). *Applied Clay Science* 160, 9–21. doi: 10.1016/j.clay.2018.02.020.

del Buey, P., Sanz-Montero, M. E., Braissant, O., Cabestrero, Ó., and Visscher, P. T. (2021). The role of microbial extracellular polymeric substances on formation of sulfate minerals and fibrous Mg-clays. *Chemical Geology* 581, 120403. doi: 10.1016/j.chemgeo.2021.120403.

Dill, H. G. (2001). The geology of aluminium phosphates and sulphates of the alunite group minerals: a review. *Earth-Science Reviews* 53, 35–93. doi: 10.1016/S0012-8252(00)00035-0.

Donovan, J. J., Allaz, J. M., von der Handt, A., Seward, G. G. E., Neill, O., Goemann, K., et al. (2021). Quantitative WDS compositional mapping using the electron microprobe. *American Mineralogist* 106, 1717–1735. doi: 10.2138/am-2021-7739.

Dos Santos, H. N., Neumann, R., and Ávila, C. A. (2017). Mineral Quantification with Simultaneous Refinement of Ca-Mg Carbonates Non-Stoichiometry by X-ray Diffraction, Rietveld Method. *Minerals* 7, 164. doi: 10.3390/min7090164.

Farmer, V. C. ed. (1974). *The Infrared Spectra of Minerals*. Mineralogical Society of Great Britain and Ireland doi: 10.1180/mono-4.

Fournelle, J., Cathey, H., Pinard, P. T., and Richter, S. (2016). Low voltage EPMA: experiments on a new frontier in microanalysis - analytical lateral resolution. *IOP Conf. Ser.: Mater. Sci. Eng.* 109, 012003. doi: 10.1088/1757-899X/109/1/012003.

Gaboreau, S., Prêt, D., Montouillout, V., Henocq, P., Robinet, J.-C., and Tournassat, C. (2017). Quantitative mineralogical mapping of hydrated low pH concrete. *Cement and Concrete Composites* 83, 360–373. doi: 10.1016/j.cemconcomp.2017.08.003.

Han, Z., Meng, R., Yan, H., Zhao, H., Han, M., Zhao, Y., et al. (2017). Calcium carbonate precipitation by Synechocystis sp. PCC6803 at different Mg/Ca molar ratios under the laboratory condition. *Carbonates Evaporites* 32, 561–575. doi: 10.1007/s13146-016-0322-5.

Hardie, L. A., and Eugster, H. P. (1970). The evolution of closed-basin brines. *Mineral.Soc.Amer.Spec* 3, 273–290.

Hombourger, C., and Outrequin, M. (2013). Quantitative Analysis and High-Resolution X-ray Mapping with a Field Emission Electron Microprobe. *Microscopy Today* 21, 10–15. doi: 10.1017/S1551929513000515.

Hughes, J. M., and Rakovan, J. (2002). The Crystal Structure of Apatite, Ca5(PO4)3(F,OH,Cl). *Reviews in Mineralogy and Geochemistry* 48, 1–12. doi: 10.2138/rmg.2002.48.1.

Kaczmarek, S. E., Gregg, J. M., Bish, D. L., Machel, H. G., Fouke, B. W., MacNeil, A., et al. (2017). Dolomite, very-high magnesium calcite, and microbes: implications for the microbial model of dolomitization. in, 7–20.

Kanaya, K., and Okayama, S. (1972). Penetration and energy-loss theory of electrons in solid targets. *Journal of Physics D: Applied Physics* 5, 43.

Katz, A., Sass, E., Starinsky, A., and Holland, H. D. (1972). Strontium behavior in the aragonite-calcite transformation: An experimental study at 40–98°C. *Geochimica et Cosmochimica Acta* 36, 481–496. doi: 10.1016/0016-7037(72)90037-3.

Keim, C. N., dos Santos, H. N., Santiago, C. S., Pennafirme, S., Neumann, R., Schnellrath, J., et al. (2020). Microstructure and mineral composition of Holocene stromatolites from Lagoa Vermelha, a hypersaline lagoon in Brazil: Insights into laminae genesis. *Journal of Sedimentary Research* 90, 887–905. doi: 10.2110/jsr.2020.40.

Kloprogge, J. T. (1999). Synthesis of Smectite Clay Minerals: A Critical Review. *Clays and Clay Minerals* 47, 529–554. doi: 10.1346/CCMN.1999.0470501.

Konhauser, K. O., and Urrutia, M. M. (1999). Bacterial clay authigenesis: a common biogeochemical process. *Chemical Geology* 161, 399–413. doi: 10.1016/S0009-2541(99)00118-7.

Lager, G. A., Armbruster, T., Rotella, F. J., Jorgensen, J. D., and Hinks, D. G. (1984). A crystallographic study of the low-temperature dehydration products of gypsum, CaSO4 · 2H2O: hemihydrate, CaSO4 · 0.50H2O, and γ-CaSO 4. *American Mineralogist* 69, 910–919.

Liu, D., Fan, Q., Papineau, D., Yu, N., Chu, Y., Wang, H., et al. (2020). Precipitation of protodolomite facilitated by sulfate-reducing bacteria: The role of capsule extracellular polymeric substances. *Chemical Geology* 533, 119415. doi: 10.1016/j.chemgeo.2019.119415.

McClellan, G. H., and Van Kauwenbergh, S. J. (1990). Mineralogy of sedimentary apatites. *Geological Society, London, Special Publications* 52, 23–31. doi: 10.1144/GSL.SP.1990.052.01.03.

Moreira, N. F., Walter, L. M., Vasconcelos, C., McKenzie, J. A., and McCall, P. J. (2004). Role of sulfide oxidation in dolomitization: Sediment and pore-water geochemistry of a modern hypersaline lagoon system. *Geol* 32, 701. doi: 10.1130/G20353.1.

Müller, G., Irion, G., and Förstner, U. (1972). Formation and Diagenesis of Inorganic Ca-Mg Carbonates. *Naturwissenschaften* 59, 158–164.

Nathan, Y. (1984). “The Mineralogy and Geochemistry of Phosphorites,” in *Photosphate Minerals*, eds. J. O. Nriagu and P. B. Moore (Berlin, Heidelberg: Springer Berlin Heidelberg), 275–291. doi: 10.1007/978-3-642-61736-2_8.

Onac, B. P., Mylroie, J. E., and White, W. B. (2001). Mineralogy of cave deposits on San Salvador Island, Bahamas. *Carbonates Evaporites* 16, 8–16. doi: 10.1007/BF03176222.

Onac, B. P., and Vereş, D. S. (2003). Sequence of secondary phosphates deposition in a karst environment: evidence from Magurici Cave (Romania). *ejm* 15, 741–745. doi: 10.1127/0935-1221/2003/0015-0741.

Pace, A., Bourillot, R., Bouton, A., Vennin, E., Braissant, O., Dupraz, C., et al. (2018). Formation of stromatolite lamina at the interface of oxygenic-anoxygenic photosynthesis. *Geobiology* 16, 378–398. doi: 10.1111/gbi.12281.

Pan, Y., and Fleet, M. E. (2002). Compositions of the Apatite-Group Minerals: Substitution Mechanisms and Controlling Factors. *Reviews in Mineralogy and Geochemistry* 48, 13–49. doi: 10.2138/rmg.2002.48.2.

Paquette, J., and Reeder, R. J. (1990). Single-crystal X-ray structure refinements of two biogenic magnesian calcite crystals. *American Mineralogist* 75, 1151–1158.

Perri, E., Gindre-Chanu, L., Caruso, A., Cefalà, M., Scopelliti, G., and Tucker, M. (2017). Microbial-mediated pre-salt carbonate deposition during the Messinian salinity crisis (Calcare di Base fm., Southern Italy). *Marine and Petroleum Geology* 88, 235–250. doi: 10.1016/j.marpetgeo.2017.08.028.

Pietzsch, R., Tosca, N. J., Gomes, J. P., Roest-Ellis, S., Sartorato, A. C. L., and Tonietto, S. N. (2022). The role of phosphate on non-skeletal carbonate production in a Cretaceous alkaline lake. *Geochimica et Cosmochimica Acta* 317, 365–394. doi: 10.1016/j.gca.2021.09.032.

Pozo, M. (2000). Origin and evolution of magnesium clays in lacustrine environments: Sedimentology and geochemical pathways. in, 117–133.

Prêt, D. (2003). Nouvelles méthodes quantitatives de cartographie de la minéralogie et de la porosité dans les matériaux argileux: application aux bentonites compactées des barrières ouvragées.

Prêt, D., Sammartino, S., Beaufort, D., Fialin, M., Sardini, P., Cosenza, P., et al. (2010a). A new method for quantitative petrography based on image processing of chemical element maps: Part II. Semi-quantitative porosity maps superimposed on mineral maps. *American Mineralogist* 95, 1389–1398. doi: 10.2138/am.2010.3433.

Prêt, D., Sammartino, S., Beaufort, D., Fialin, M., Sardini, P., Cosenza, P., et al. (2010b). A new method for quantitative petrography based on image processing of chemical element maps: Part II. Semi-quantitative porosity maps superimposed on mineral maps. *American Mineralogist* 95, 1389–1398. doi: 10.2138/am.2010.3433.

Prêt, D., Sammartino, S., Beaufort, D., Meunier, A., Fialin, M., and Michot, L. J. (2010c). A new method for quantitative petrography based on image processing of chemical element maps: Part I. Mineral mapping applied to compacted bentonites. *American Mineralogist* 95, 1379–1388. doi: 10.2138/am.2010.3431.

Prêt, D., Sammartino, S., Beaufort, D., Meunier, A., Fialin, M., and Michot, L. J. (2010d). A new method for quantitative petrography based on image processing of chemical element maps: Part I. Mineral mapping applied to compacted bentonites. *American Mineralogist* 95, 1379–1388. doi: 10.2138/am.2010.3431.

Raz, S., Weiner, S., and Addadi, L. (2000). Formation of High-Magnesian Calcites via an Amorphous Precursor Phase: Possible Biological Implications. *Adv. Mater.* 12, 38–42. doi: 10.1002/(SICI)1521-4095(200001)12:1<38::AID-ADMA38>3.0.CO;2-I.

Ries, J. B., Anderson, M. A., and Hill, R. T. (2008). Seawater Mg/Ca controls polymorph mineralogy of microbial $CaCO_3$: A potential proxy for calcite-aragonite seas in Precambrian time. *Geobiology* 6, 106–119. doi: 10.1111/j.1472-4669.2007.00134.x.

Rousseau, R. (2013). How to Apply the Fundamental Parameters Method to the Quantitative X-ray Fluorescence Analysis of Geological Materials. *Journal of Geosciences and Geomatics* 1, 1–7. doi: 10.12691/jgg-1-1-1.

Russ, J. C. (1999). *The image processing handbook.* 3rd ed. Boca Raton: CRC press.

Saint Martin, J.-P., and Saint Martin, S. (2015). Discovery of calcareous microbialites in coastal ponds of western Sardinia (Italy). *Geo-Eco-Marina* 21, 35–53.

Samylina, O. S., and Zaytseva, L. V. (2019). Characterization of modern dolomite stromatolites from hypersaline Petukhovskoe Soda Lake, Russia. *Lethaia* 52, 1–13. doi: 10.1111/let.12286.

Sherman, J. (1955). The theoretical derivation of fluorescent X-ray intensities from mixtures. *Spectrochimica Acta* 7, 283–306. doi: 10.1016/0371-1951(55)80041-0.

Siegel, F. R. (1960). The effect of strontium on the aragonite-calcite ratios of Pleistocene corals [Florida]. *Journal of Sedimentary Research* 30, 297–304. doi: 10.1306/74D70A24-2B21-11D7-8648000102C1865D.

Souza-Egipsy, V., Wierzchos, J., Ascaso, C., and Nealson, K. H. (2005). Mg–silica precipitation in fossilization mechanisms of sand tufa endolithic microbial community, Mono Lake (California). *Chemical Geology* 217, 77–87. doi: 10.1016/j.chemgeo.2004.12.004.

Spadafora, A., Perri, E., Mckenzie, J. A., and Vasconcelos, C. (2010). Microbial biomineralization processes forming modern Ca:Mg carbonate stromatolites:

Biomineralization processes forming stromatolites. *Sedimentology* 57, 27–40. doi: 10.1111/j.1365-3091.2009.01083.x.

Stanienda-Pilecki, K. J. (2018). Magnesium calcite in Muschelkalk limestones of the Polish part of the Germanic Basin. *Carbonates and Evaporites* 33, 801–821. doi: 10.1007/s13146-018-0437-y.

Stephenson, A. E., DeYoreo, J. J., Wu, L., Wu, K. J., Hoyer, J., and Dove, P. M. (2008). Peptides Enhance Magnesium Signature in Calcite: Insights into Origins of Vital Effects. *Science* 322, 724–727. doi: 10.1126/science.1159417.

Theye, T., and Seidel, E. (1993). Uplift-related retrogression history of aragonite marbles in western Crete (Greece). *Contributions to Mineralogy and Petrology* 114, 349–356.

Tosca, N. J. ., and Masterson, A. L. (2014). Chemical controls on incipient Mg-silicate crystallization at 25°C: Implications for early and late diagenesis. *Clay miner.* 49, 165–194. doi: 10.1180/claymin.2014.049.2.03.

Tosca, N. J., McLennan, S. M., Lamb, M. P., and Grotzinger, J. P. (2011). Physicochemical properties of concentrated Martian surface waters. *J. Geophys. Res.* 116, E05004. doi: 10.1029/2010JE003700.

van Lith, Y., Vasconcelos, C., Warthmann, R., Martins, J. C. F., and McKenzie, J. A. (2002). Bacterial sulfate reduction and salinity: two controls on dolomite precipitation in Lagoa Vermelha and Brejo do Espinho (Brazil). *Hydrobiologia* 485, 35–49. doi: 10.1023/A:1021323425591.

Van Lith, Y., Warthmann, R., Vasconcelos, C., and Mckenzie, J. A. (2003). Sulphate-reducing bacteria induce low-temperature Ca-dolomite and high Mg-calcite formation. *Geobiology* 1, 71–79. doi: 10.1046/j.1472-4669.2003.00003.x.

Vasconcelos, C., Dittrich, M., and McKenzie, J. A. (2014). Evidence of microbiocoenosis in the formation of laminae in modern stromatolites. *Facies* 60, 3–13. doi: 10.1007/s10347-013-0371-3.

Vasconcelos, C., and McKenzie, J. A. (1997). Microbial Mediation of Modern Dolomite Precipitation and Diagenesis Under Anoxic Conditions (Lagoa Vermelha, Rio de Janeiro, Brazil). *SEPM JSR* Vol. 67. doi: 10.1306/D4268577-2B26-11D7-8648000102C1865D.

Vasconcelos, C., Warthmann, R., McKenzie, J. A., Visscher, P. T., Bittermann, A. G., and van Lith, Y. (2006). Lithifying microbial mats in Lagoa Vermelha, Brazil: Modern Precambrian relics? *Sedimentary Geology* 185, 175–183. doi: 10.1016/j.sedgeo.2005.12.022.

Wang, D., Wallace, A. F., De Yoreo, J. J., and Dove, P. M. (2009). Carboxylated molecules regulate magnesium content of amorphous calcium carbonates during calcification. *Proceedings of the National Academy of Sciences* 106, 21511–21516. doi: 10.1073/pnas.0906741106.

Zanetta, P.-M., Le Guillou, C., Leroux, H., Zanda, B., Hewins, R. H., Lewin, E., et al. (2019). Modal abundance, density and chemistry of micrometer-sized assemblages by advanced electron microscopy: Application to chondrites. *Chemical Geology* 514, 27–41. doi: 10.1016/j.chemgeo.2019.03.025.

Zeyen, N., Benzerara, K., Beyssac, O., Daval, D., Muller, E., Thomazo, C., et al. (2021). Integrative analysis of the mineralogical and chemical composition of modern microbialites from ten Mexican lakes: What do we learn about their formation? *Geochimica et Cosmochimica Acta* 305, 148–184. doi: 10.1016/j.gca.2021.04.030.

Zeyen, N., Benzerara, K., Li, J., Groleau, A., Balan, E., Robert, J.-L., et al. (2015). Formation of low-T hydrated silicates in modern microbialites from Mexico and implications for microbial fossilization. *Front. Earth Sci.* 3. doi: 10.3389/feart.2015.00064.

Zhang, F., Xu, H., Shelobolina, E. S., Konishi, H., Converse, B., Shen, Z., et al. (2015). The catalytic effect of bound extracellular polymeric substances excreted by anaerobic microorganisms on Ca-Mg carbonate precipitation: Implications for the “dolomite problem.” *American Mineralogist* 100, 483–494. doi: 10.2138/am-2015-4999.

1.1.1 Supplementary Materials

Table S1. Precisions of the bulk chemical ICP-AES measurements for the major elements depending on their wt% (first column).

ICP-OES iCap6500	**SiO2**	**Al2O3**	**Fe2O3**	**MnO**	**MgO**	**CaO**	**Na2O**	**K2O**	**TiO2**	**P2O5**
>10 %	<2%	<2%	<2%			<2%				
>5 %		<10%			<2%	<5%	<5%	<5%	<5%	
>1 %		<15%	<10%	<5%	<10%		<10%	<10%	<10%	<5%
>0.5 %	<10%		<15%	<15%	<15%	<15%	<15%	<20%	<20%	<15%
>0.1 %	<20%	<20%								**
>0.05 %	**	**	<20%	<20%	<20%	<25%	<25%	<25%	<25%	
>0.01 %			**	**	**	**	**	**	**	
L.D. %	0.05	0.04	0.015	0.015	0.03	0.03	0.02	0.03	0.02	0.10

Table S2. Theoretical endmembers used in the µphasemap software

Abbreviations	**Mineral name**	**Theoretical composition**
Calc	Calcite	$Ca_1C_1O_3$
Calc 1	Calcite 1	$(Ca_{0.95}Mg_{0.05})C_1O_3$
Calc 2	Calcite 2	$(Ca_{0.85}Mg_{0.15})C_1O_3$
Calc 3	Calcite 3	$(Ca_{0.7}Mg_{0.3})C_1O_3$
Dolo	Dolomite	$(Ca_{0.5}Mg_{0.5})C1O3$
P-apatite	Apatite	$Ca_5(PO_4)_3(OH)_1$
Ces	Cesanite	$Ca_5(SO_4)_3(OH)_1$
Gy	Gypsum	$Ca_1S_1O_4$
woodhouseite	woodhouseite	$Ca_1Al_3(PO_4SO_4)(OH)_6$
Quartz	Quartz	Si_1O_2
Ort	Orthose	$K_1Al_1Si_3O_8$
Alb	Albite	$Na_1Al_1\ Si_3O_8$
Anor	Anorthite	$Ca_1Al_1Si_2O_8$
Kaol	Kaolinite	$Al_2Si_2O_5(OH)_4$
Serp	Serpentine	$Mg_3Si_2O_5(OH)_4$
Talc	Talc	$Mg_3Si_4O_{10}(OH)_2$
Sep	Sepiolite	$Mg_{2.66}Si_4O_{10}(OH)_{2.66}$
SepNa	SepioliteNa	$Mg_{2.33}Na_{0.66}Si_4O_{10}(OH)_{2.66}$
Musc	Muscovite	$K_1Al_2(AlSi_3)O_{10}(OH)_2$
Cel	Celadonite	$K_1(Mg_1Al_1)Si_4O_{10}(OH)_2$
Phlo	Phlogopite	$K_1Mg_3(Al_1Si_3)O_{10}(OH)_2$
Glau	Biotiteglauconite	$K_{0.8}(Fe)_2(Si_{3.7}Al_{0.3})O_{10}(OH)_2$
Bei	Beidellite	$Na_{0.3}Al_2(Si_{3.7}Al_{0.3})O_{10}(OH)_2$
Mont	Montmorillonite	$Na_{0.3}(Al_{1.7}Mg_{0.3})(Si_4)O_{10}(OH)_2$
Stev	Stevensite	$Na_{0.5}Mg_{2.5}(Si_4)O_{10}(OH)_2$
SapMg	SaponiteMginter	$Mg_{0.25}Mg_3(Si_{3.5}Al_{0.5})O_{10}(OH)_2$
SapK	SaponiteMgKinter	$K_{0.5}Mg_3(Si_{3.5}Al_{0.5})O_{10}(OH)_2$
Cham	Chamoisite	$(Fe_2Al_1)(OH)_6(Si_3Al_1)Fe_3O_{10}(OH)_2$
Chlo	Chloriteditri	$(Mg_2Al_1)(OH)_6(Si_3Al_1)Mg_3O_{10}(OH)_2$
Marg	Marguarite	$Ca_1Al_2(Al_2Si_2)O_{10}(OH)_2$

Table S3. Chemical composition of the Mari Ermi waters (unpublished data)

pH	Salinity	Ca^{2+} mM	K^{+} mM	Mg^{2+} mM	Na^{+} mM	Sr^{2+} mM	H_4SiO_4 mM	Br- mM
9.1	42.9	12.15	11.99	59.05	536.83	0.103	0.070	2.69

HCO_3^- mM	CO_3^{2-} mM	Cl^- mM	PO_4^{3-} mM	SO_4^{2-} mM	∑cations mM	∑anions mM	Bal %
0.8712	0.061	627.13	0.0013	29.85	620.13	660.60	-3.16

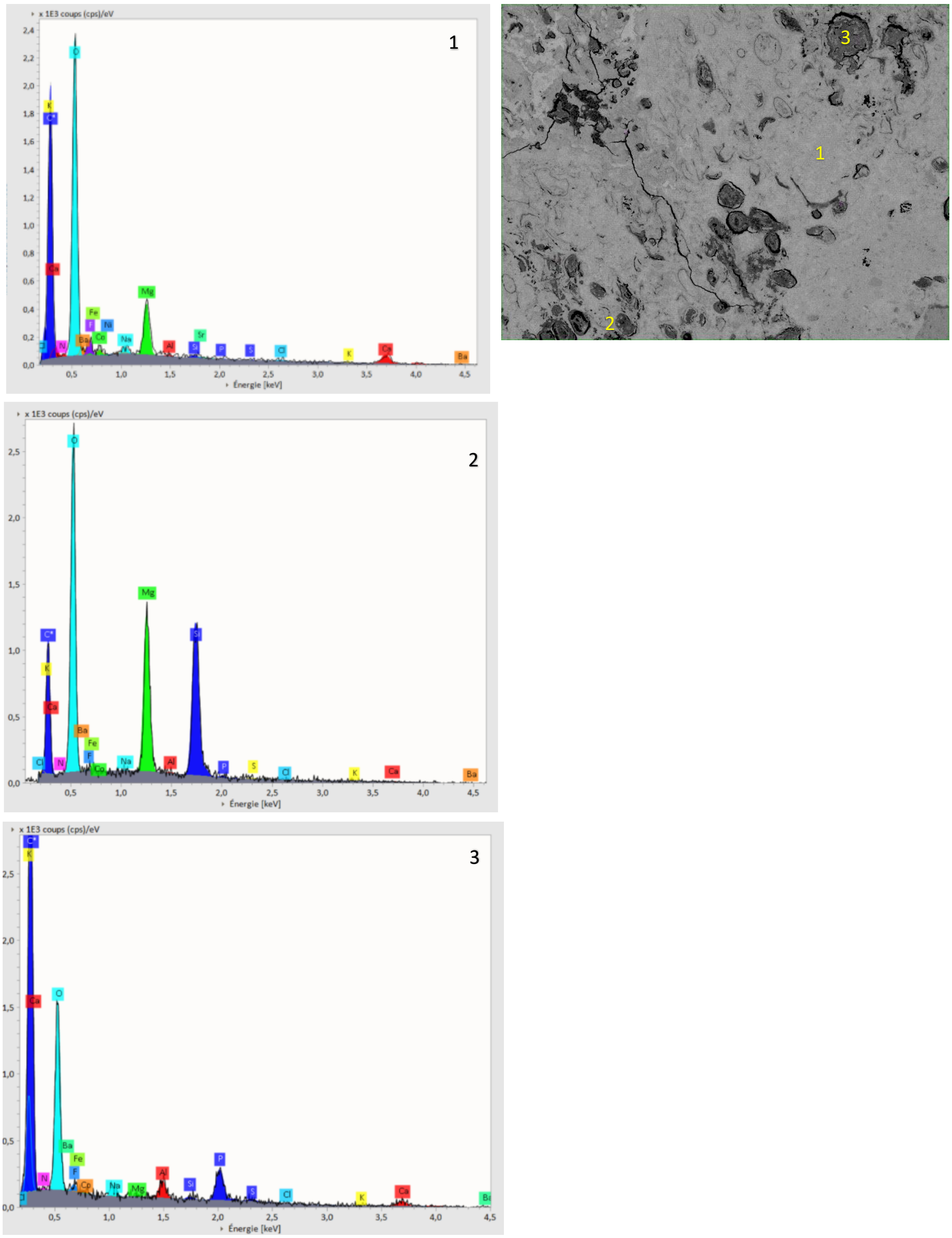

Fig. S1. 1-pixel EDX quantified spectra located in different mineral phase (1 and 2) and in porosities (3) to cross validate the EDX quantification method.

Fig. S2. BSE mosaic (html file)

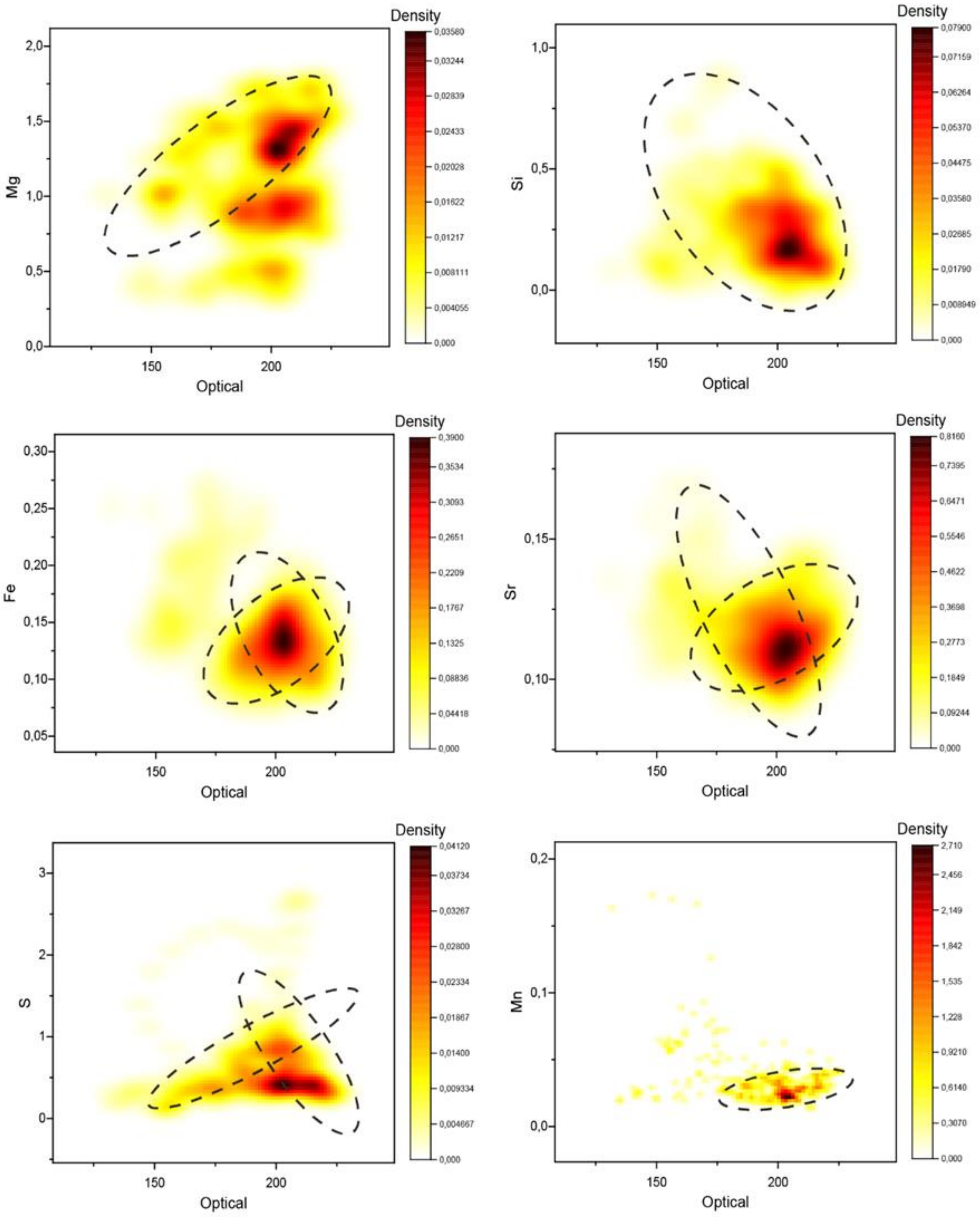

Fig. S3. 2D-kernel density scatter plots highlighting correlations between (on y axes) the gray values from an optical image and (on x axis) elemental concentrations retrieved from the same pixels in µXRF maps. The optical image and x-ray maps were obtained at the same time, using the same XRF instrument. The optical image is shown in Table 2 and x-ray maps in Figure 5. Grey values and x-ray intensities for the different chemical elements were retrieved from one rectangle drawn using FIJI on the optical image and the x-ray maps along a transect drawn perpendicularly to the dark and bright laminae.

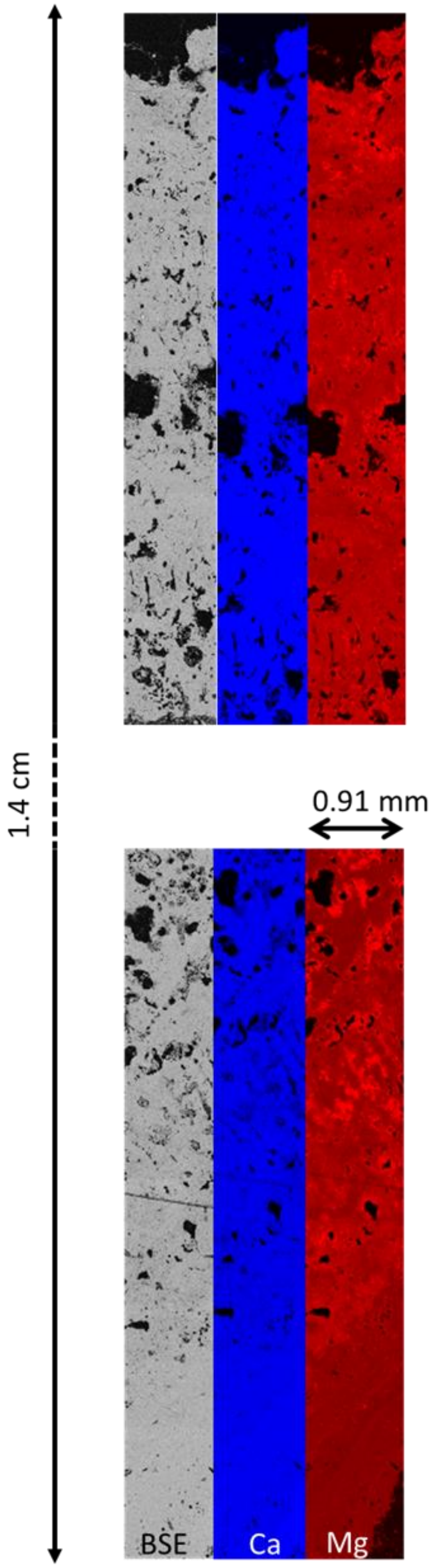

Fig. S4. SEM-EDXS mosaic showing the distribution of Mg and Ca along a profile across a Mari Ermi stromatolite. (a) SEM-BSE image. The substrate appears at the bottom right hand corner of the image and the top surface of the stromatolite at the top of the image. (b) Calcium raw count map. (c) Magnesium raw count map. Note that the Mg heterogeneities in calcite distributed along the laminae.

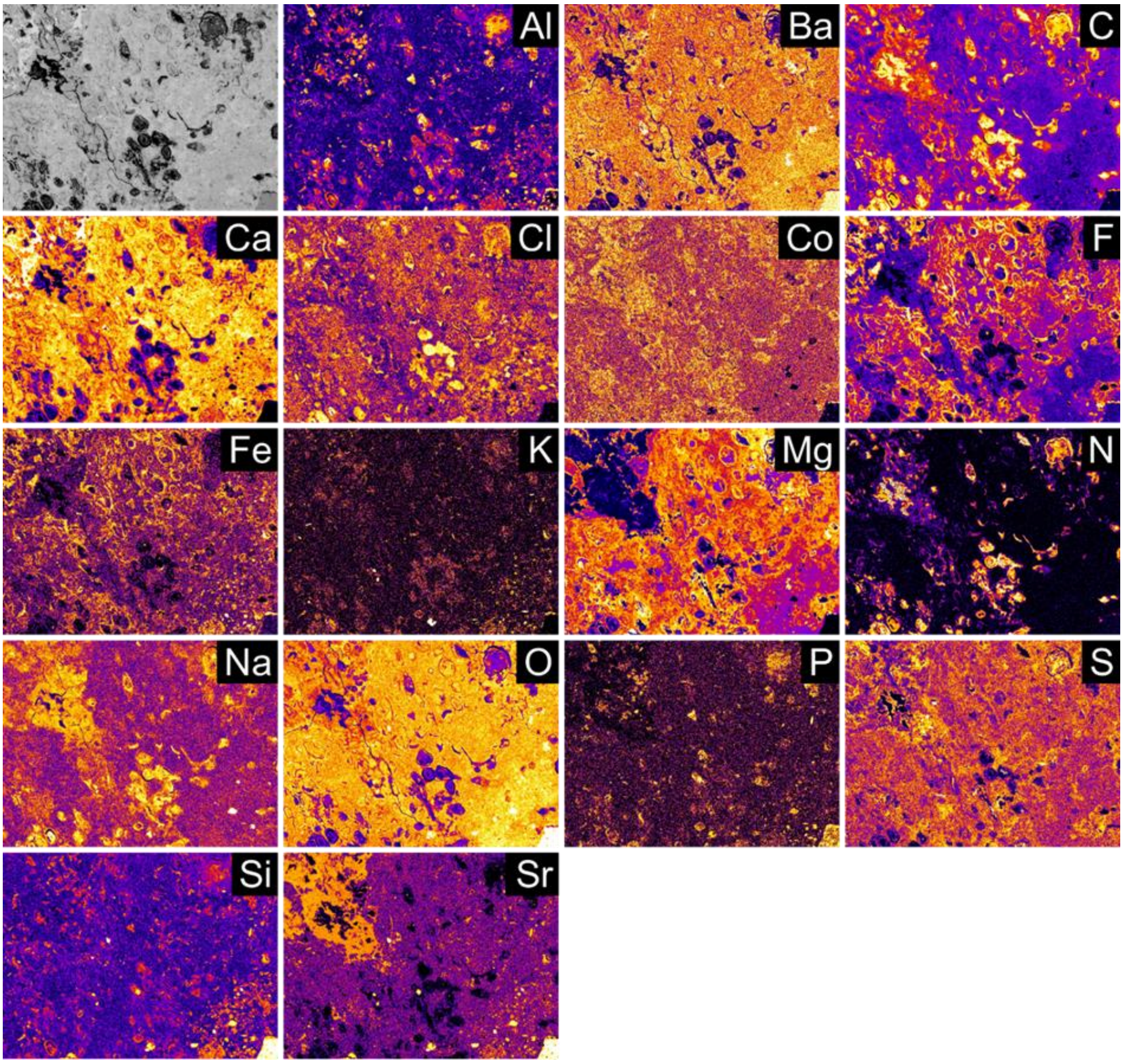

Fig. S5. Quantified SEM-EDXS maps of Al, Ba, Ca, Cl, Co, F, Fe, K, Mg, N, Na, O, P, S, Si, Sr encoded with histogram equalization to enhance the contrast.

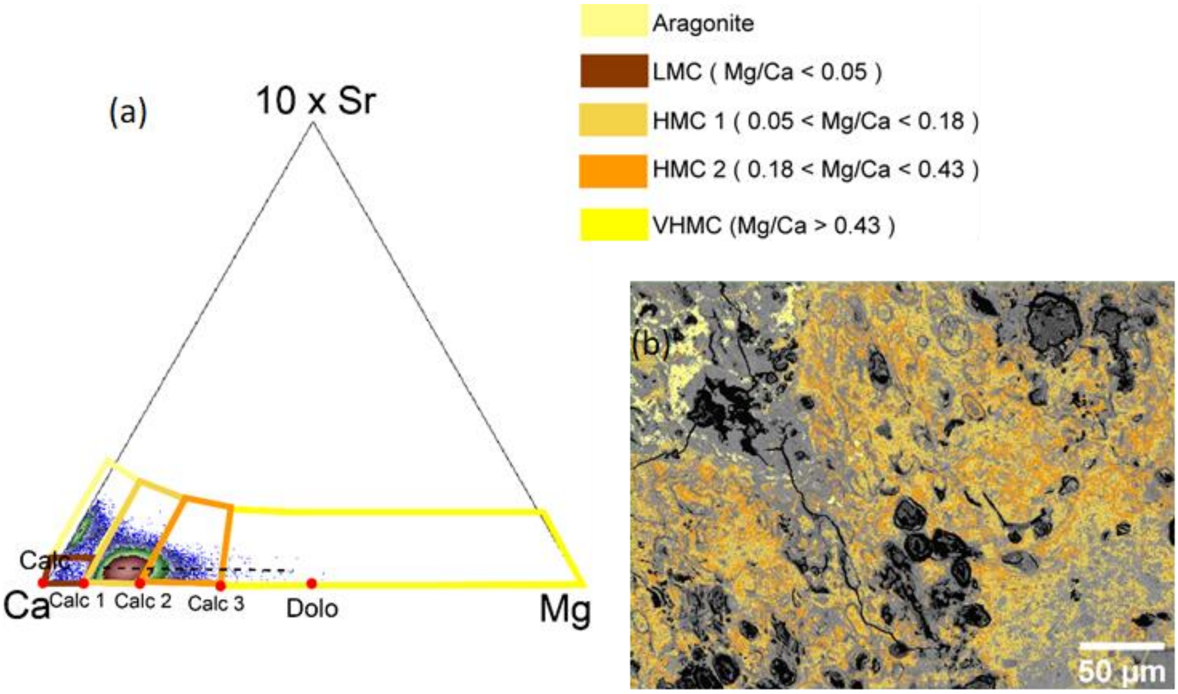

Fig. S6. Study of the pure carbonate cluster segmentation (a) 10Sr – Ca – Mg ternary diagram containing the pixels coming from the pure carbonate cluster extracted from Fig. 8a. Note that no pixel with a Mg content higher than that of dolomite is observed. (b) Back projection of the carbonate pixels in the BSE.

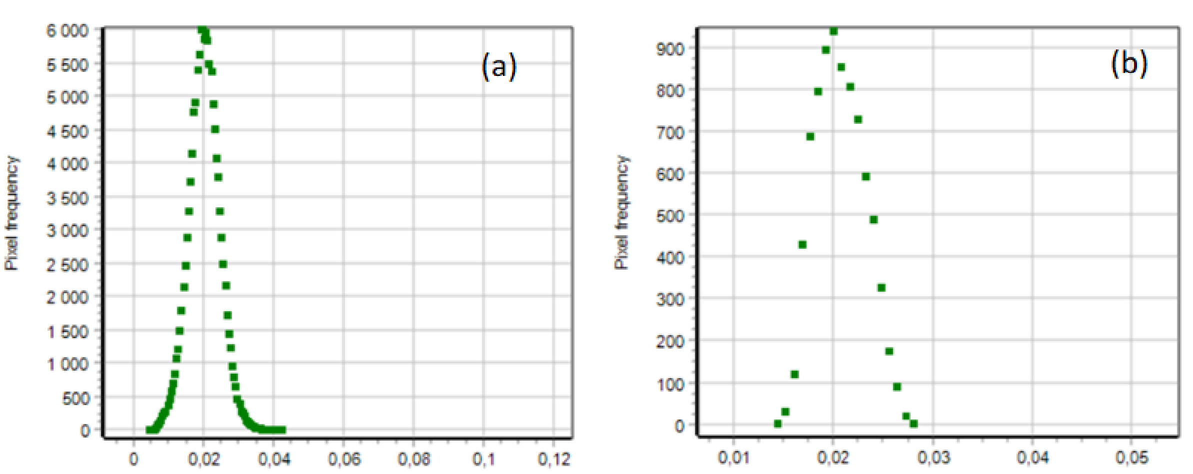

Fig. S7 Frequency histogram of the number of Sr atoms per formula unit (p.f.u) in the (a) porous aragonite phase and (b) non-porous aragonite phase. Note that both normal distributions are centered at 0.02 Sr atom p.f.u. and range between 0.015 and 0.03.

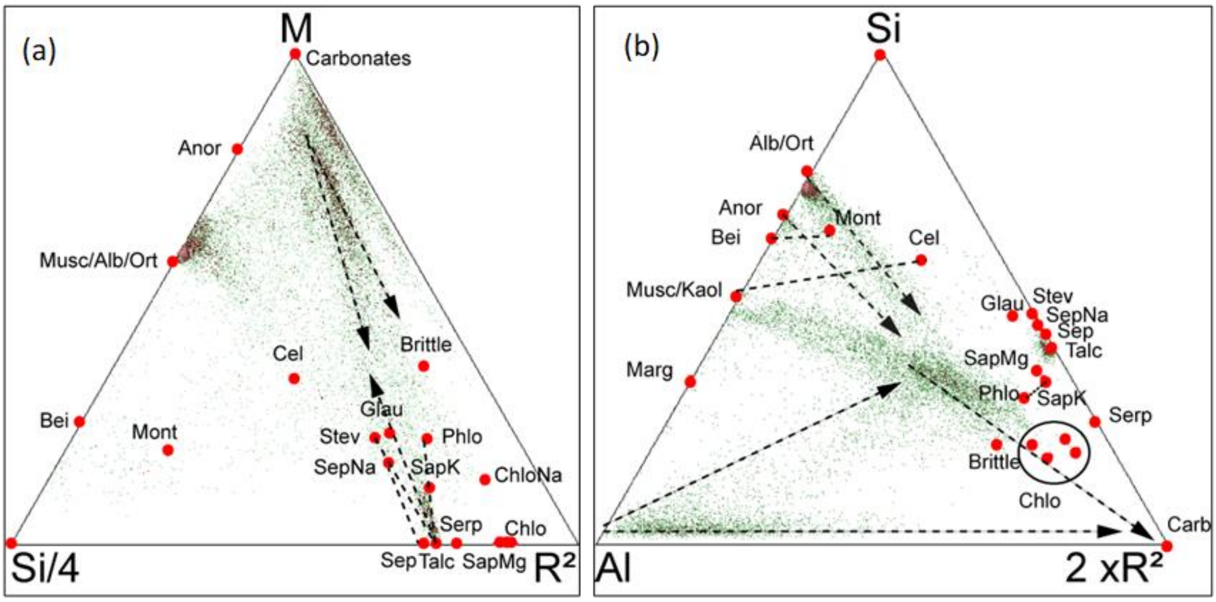

Fig. S7. Additional ternary plots. (a) M-Si/4-R^2 diagram shows that Mg-phyllosilicate composition match with talc and not with serpentine or sepiolite. Note that the talc cluster is stretched between either glauconite or an in-between stevensite - saponite phase. (b) Si-Al-R^2 diagram shows that the mixture talc/glauconite is unlikely since there is no pixels around glauconite endmembers. R2 = Mg (mol%) + Fe (mol%)

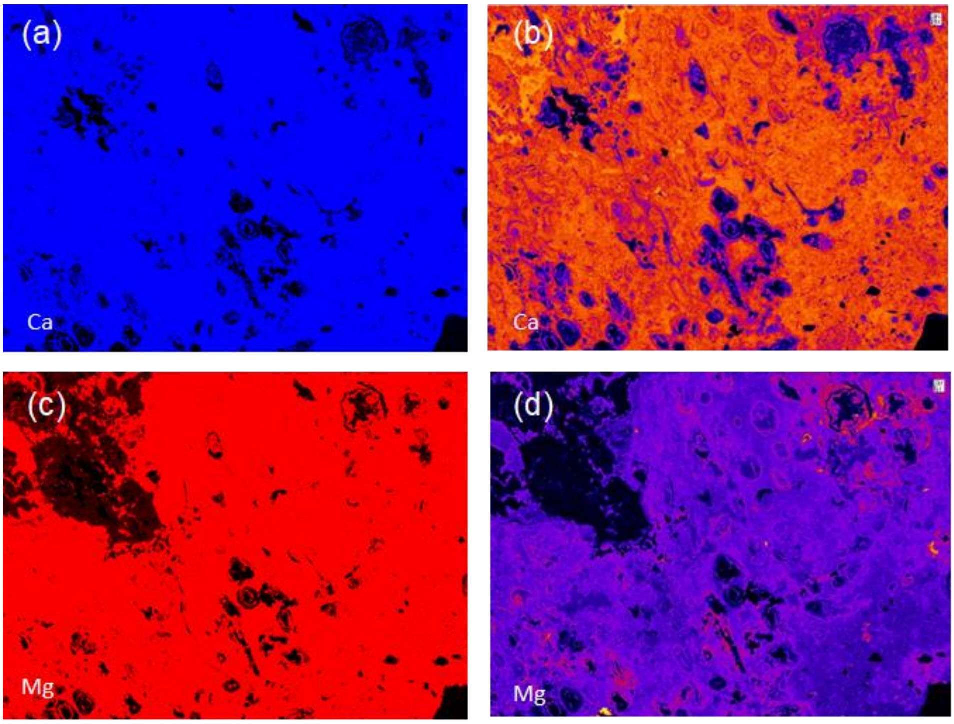

Fig. S9. Study raw EDX map vs quantified EDX maps. (a) Raw count Ca map vs (b) Ca-quantified map (c) Raw count Mg map vs (d) Mg-quantified map. The raw maps come from the Bruker software where an automatic contrast is applied.